J. Fluid Mech. (2001), *vol.* 433, *pp.* 251–281. Printed in the United Kingdom

Dynamics of laser-induced cavitation bubbles near an elastic boundary

By EMIL-ALEXANDRU BRUJAN†, KESTER NAHEN, PETER SCHMIDT AND ALFRED VOGEL‡

Medical Laser Center Lübeck, Peter-Monnik-Weg 4, D-23562 Lübeck, Germany

(Received 21 February 2000 and in revised form 23 October 2000)

The interaction of a laser-induced cavitation bubble with an elastic boundary and its dependence on the distance between bubble and boundary are investigated experimentally. The elastic boundary consists of a transparent polyacrylamide (PAA) gel with 80% water concentration with elastic modulus $E = 0.25$ MPa. At this E-value, the deformation and rebound of the boundary is very pronounced providing particularly interesting features of bubble dynamics. It is shown by means of high-speed photography with up to 5 million frames s^{-1} that bubble splitting, formation of liquid jets away from and towards the boundary, and jet-like ejection of the boundary material into the liquid are the main features of this interaction. The maximum liquid jet velocity measured was 960 m s^{-1}. Such high-velocity jets penetrate the elastic boundary even through a water layer of 0.35 mm thickness. The jetting behaviour arises from the interaction between the counteracting forces induced by the rebound of the elastic boundary and the Bjerknes attraction force towards the boundary. General principles of the formation of annular and axial jets are discussed which allow the interpretation of the complex dynamics. The concept of the Kelvin impulse is examined with regard to bubble migration and jet formation. The results are discussed with respect to cavitation erosion, collateral damage in laser surgery, and cavitation-mediated enhancement of pulsed laser ablation of tissue.

1. Introduction

Interest in the dynamics of cavitation bubbles near a compliant elastic boundary was initially stimulated by the observation of Gibson (1968) that, under certain conditions, the liquid jet formed during bubble collapse as well as the bubble migration are both directed away from the boundary. Since jet impact and the high pressures developed during bubble collapse near a rigid boundary were already known as major factors causing cavitation erosion (Naudé & Ellis 1961; Benjamin & Ellis 1966), the use of compliant boundaries was considered as a means to prevent erosion. The studies on bubble interaction with elastic boundaries focused for quite some time on investigation of integral properties of bubble dynamics (such as, for example, the Kelvin impulse) to determine the direction of bubble migration and jet formation. Much research was performed on elastic materials composed of layered structures. Gibson & Blake (1980, 1982) and Blake & Gibson (1987) examined the behaviour of spark-generated bubbles in the vicinity of rigid boundaries with rubber coatings. They also performed a limited

† Present address: Department of Hydraulics, University Politechnica, Spl. Independentei 313, 77206 Bucharest, Romania (e-mail: brujan@chmh.hydrop.pub.ro)

‡ Author to whom correspondence should be addressed; e-mail: vogel@mll.mu-luebeck.de

number of experiments to investigate the influence of some physical properties of the composite surface, namely surface inertia and stiffness, on the bubble behaviour. A very interesting observation was that, for some range of coating properties, no re-entrant jet is developed during bubble collapse, neither towards nor away from the boundary. In this case, the bubble collapses from its sides forming an hour-glass shape which can eventually lead to bubble splitting. However, no details of the motion after the bubble splitting were presented.

In a more recent study, Shima *et al.* (1989) investigated the migratory characteristics of spark-generated bubbles near planar composite surfaces consisting of two viscoelastic materials. They noted that, with an appropriate combination of surface stiffness and inertia, a neutral bubble collapse, characterized by no migration towards or away from a boundary, can be obtained at a certain distance between bubble and boundary. A part of their experimental results has been theoretically confirmed by Duncan and co-workers (Duncan & Zhang 1991; Duncan, Milligan & Zhang 1996).

Recently Shaw *et al.* (1999) investigated the interaction of a laser-generated cavitation bubble with a flexible membrane and Kodama & Tomita (2000) studied the bubble dynamics near gelatine surfaces. These studies were, however, mostly restricted to the case when the bubble is generated at a relatively large distance from the boundary (larger than or on the order of its maximum radius). An extension of these studies to investigate the dynamical behaviour of a bubble situated very close to an elastic boundary is, therefore, highly desirable for a better understanding of the cavitation phenomena, including the jetting dynamics and the possible cavitation damage to nearby surfaces.

In the last few years, the interaction between cavitation bubbles and elastic boundaries has become very important in the context of medical laser applications. Whenever short laser pulses are used to ablate or disrupt tissue in a liquid environment, cavitation bubbles are produced which interact with the tissue. This situation is encountered in various applications of laser surgery, such as intraocular photodisruption (Steinert & Puliafito 1985; Vogel 1997), laser angioplasty (Deckelbaum 1994), laser thrombolysis (Gregory 1994), myocardial laser revascularization (Klein, Schulte & Gams 1998; Brinkmann *et al.* 1999) and arthroscopic cartilage ablation (Smith 1993). The interaction between cavitation bubbles and tissue during pulsed laser ablation and photodisruption may cause collateral damage to sensitive tissue structures in the vicinity of the laser focus (Vogel *et al.* 1990), and it may also contribute in several ways to ablation and cutting: by disruption caused during bubble expansion, by jetting towards the boundary, by tensile stress exerted during bubble collapse, or by the elastic-plastic response of the deformed tissue. In any case, a characterization of the interaction is of interest for an optimization of the surgical procedure.

The present study describes systematic experimental investigations of the dynamics of a laser-induced cavitation bubble near the boundary of a homogeneous elastic material. The elastic boundary consists of a transparent polyacrylamide (PAA) gel with elastic modulus at 10% strain $E = 0.25$ MPa. In this choice we have been guided by the observation that the elastic response of that boundary to the bubble-induced deformation is very pronounced providing interesting and new features of the bubble dynamics which differ strongly from the dynamics near a rigid boundary. The elastic modulus of the PAA gel resembles the elastic properties of various biological tissues, such as thoracic aorta (0.04–0.9 MPa) (Fung 1993; Duck 1990), articular cartilage (0.4–0.85 MPa), muscle (0.06–0.8 MPa) (Duck 1990), and cornea (0.3–5 MPa) (Hoeltzel *et al.* 1992). A range of E-values is quoted here for each tissue type, because the elastic modulus of biological tissue depends strongly on the applied stress.

The cavitation bubble dynamics and the deformation of the boundary were examined by high-speed photography and acoustic measurements. The overall motion of the bubble was investigated by high-speed photography with 50 000 frames s^{-1} and the collapse phase with 1 million and 5 million frames s^{-1}. Diffuse illumination was used to observe the interior of the bubble while parallel illumination provided the optimal contrast for the observation of the boundary deformation, shock wave emission and liquid jet penetration into the boundary.

The parameter varied in the present study is the non-dimensional stand-off parameter, defined as the distance s between the laser focus and the boundary scaled by the maximum bubble radius R_{max}. This parameter is denoted here by γ. In a follow-up paper (Brujan *et al.* 2001) the investigations are extended to the dependence on the elastic modulus E. With decreasing E-value, the bubble dynamics approaches the limit of an infinite fluid and with increasing E-value, it is more similar to the case of a rigid boundary. The present paper reveals fundamental principles of the interaction between bubbles and elastic boundaries which are in the follow-up paper used to interpret the highly variable behaviour in the whole (E, γ)-space.

We found that the bubble–boundary interaction is very complex, with a sensitive dependence on the bubble–boundary distance, and cannot be adequately described in terms of an integral parameter such as the Kelvin impulse. For large γ-values, we observed an axial jet flow directed away from the boundary. In a large part of the parameter space, however, annular jets are formed which first lead to bubble splitting and then result in fast axial jets flowing in opposite directions. These jets reach maximum velocities of up to 960 m s^{-1} in the direction towards the boundary and up to 600 m s^{-1} in the opposite direction, even though the value of the Kelvin impulse of the whole two-bubble system is relatively small or even zero. For small γ-values, the elastic deformation of the boundary results in a jet-like ejection of boundary material into the surrounding liquid – a phenomenon which was recently reported by Chapyak & Godwin (1998) in the context of laser thrombolysis.

The results of our investigation are discussed with respect to cavitation erosion, collateral damage in laser surgery and cavitation-mediated enhancement of tissue ablation and tissue cutting.

2. Methods

2.1. *Bubble generation*

A schematic diagram depicting the experimental arrangement used for investigating the behaviour of a laser-induced cavitation bubble near an elastic boundary is shown in figure 1. The bubbles were generated in a glass cuvette filled with doubly distilled water by using a Q-switched Nd:YAG laser (Continuum YG 671-10). The laser delivered light pulses at a wavelength of 1064 nm with energies of up to 250 mJ and a pulse duration of 6 ns. The laser beam was first expanded by a telescope consisting of a biconcave lens ($f = -40$ mm) and a Nd:YAG laser achromat ($f = 200$ mm) to allow a large focusing angle together with a large distance between focus and cuvette walls. A second Nd:YAG laser achromat ($f = 125$ mm) focused the laser pulses into the glass cuvette. Achromats were used for beam collimation and focusing to minimize spherical aberrations, and for the same purpose an ophthalmic contact lens corrected for an air–water transition (Rodenstock RYM) was built into the cuvette wall (Vogel, Busch & Parlitz 1996*a*). Aiming was facilitated by a helium–neon laser beam coupled into the beam path of the Nd:YAG laser. The laser focus coincided

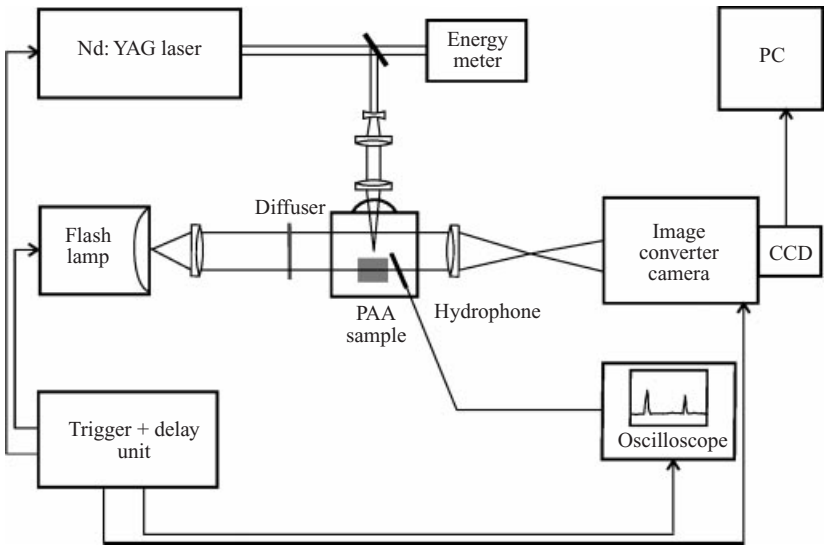

FIGURE 1. Experimental arrangement for the investigation of the behaviour of a laser-induced bubble near an elastic boundary (PAA sample).

with the aplanatic point of the contact lens, and the convergence angle of the laser beam in water was 32°. The large focusing angle was chosen to produce compact plasmas and, hence, spherical bubbles. The smooth beam profile and the minimization of aberrations ensured that no 'hot spots' occurred in the focal region of the laser beam and only one single plasma was formed. During each laser exposure, the pulse energy was measured using a pyroelectric energy meter (Laser Precision Rj 7100). The pulse-to-pulse fluctuations of the laser energy were in the range of $\pm 3\%$. The direction of the laser light was perpendicular to the elastic boundary. According to Vogel *et al.* (1996*b*), the plasma generated in the focus of a nanosecond laser pulse fills the complete cone angle of the laser beam proximal to the laser while the region beyond the laser focus is shielded by the absorption of the laser light in the plasma. Thus, a direct interaction between plasma and boundary can be excluded even if the distance between laser focus and boundary is very small.

2.2. *Elastic boundary*

The elastic boundary consisted of a transparent polyacrylamide (PAA) gel with 80% water content. PAA is the material usually used for gel electrophoresis. To produce the PAA samples 40 g of acrylamide and 1.1 g of bis-acrylamide were mixed with 160 g of 0.22 M aqueous Tris buffer (pH 9.5). After degassing, the solution was mixed with 1 ml 10% ammoniumpersulphate (APS). The solution was then placed in a plastic container and mixed with 0.2 ml N,N,N′,N′-tetramethylethylenediamine (TEMED) to initiate polymerization. A plastic grid was placed in the container to allow the simultaneous production of 49 PAA samples with flat surfaces. All components for the PAA preparation were obtained from BioRad Laboratories. The samples were left overnight to ensure good polymerization. The thickness of the PAA sample was 20 mm and the area of the surface exposed to the bubble was $15 \times 15\,\mathrm{mm}^2$. The density of the PAA was $\rho_s = 1050\,\mathrm{kg\,m^{-3}}$. The sample was mounted in a Teflon holder and completely immersed in water during the experiment. In order to avoid permeation of water into the sample and any perturbations of the bubble dynamics

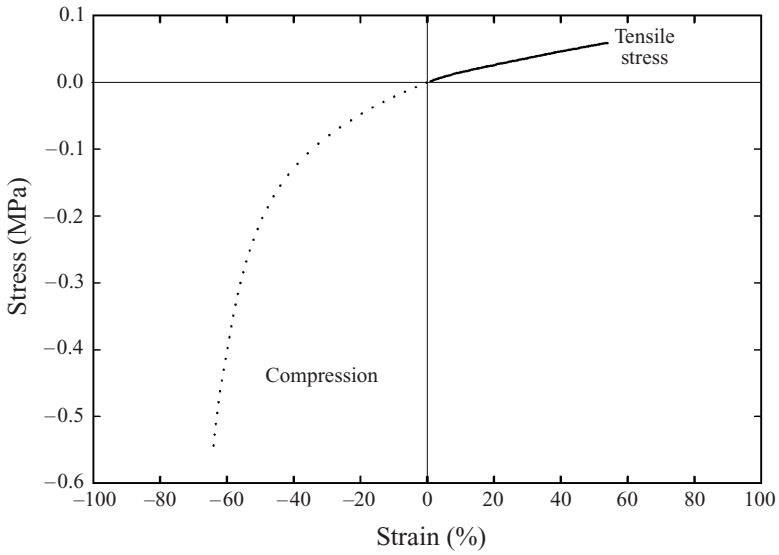

FIGURE 2. Stress–strain curve for PAA with 80% water content under tensile and compressive load. The curves were recorded with a strain rate of $\dot{\varepsilon} = 1.7 \times 10^{-3}\,\mathrm{s}^{-1}$ (a deformation of 1 mm min^{-1} was applied to 10 mm long specimens) until mechanical failure of the specimen occurred.

caused by remnant deformations of the boundary, a new sample was used for every laser exposure.

We determined the complete stress–strain curve of the PAA material under uniaxial compressive and tensile load up to mechanical failure (figure 2). A constant deformation rate of 1 mm min^{-1} was applied to 10 mm long specimens using a universal testing machine (Zwick 1456). The resulting strain rate was $\dot{\varepsilon} = 1.7 \times 10^{-3}\,\mathrm{s}^{-1}$. Young's modulus at 10% compressive strain was found to be $E = 0.25$ MPa. A strain of up to 60% could be achieved under tensile load before the sample broke. The ultimate tensile strength was $Y = 0.056$ MPa. Under compression, the sample broke at a stress value of $Y = 0.54$ MPa. In both cases, failure probably starts at micro-cracks or other tiny irregularities at the surface of the sample. It should be noted that the ultimate tensile strength of many soft biological tissues is about one order of magnitude larger than that measured for PAA, even though the elastic modulus is quite similar (Duck 1990). Furthermore, tissue usually becomes stiffer with increasing tensile load whereas PAA, like most polymers, becomes more compliant. When the deformation rate in the compression tests was increased from 1 mm min^{-1} to 1 m min^{-1} ($\dot{\varepsilon} = 1.7\,\mathrm{s}^{-1}$), the elastic modulus increased from $E = 0.25$ MPa to $E = 0.28$ MPa. The dependence of the elastic modulus on the deformation rate indicates that the E-values given in table 1 in Brujan *et al.* (2001) are lower estimates of the values relevant for the cavitation bubble dynamics near PAA samples where strain rates of the order of $10^5\,\mathrm{s}^{-1}$ may be reached.

2.3. *High-speed photography*

The dynamics of the cavitation bubble was recorded with a high-speed image converter camera (Hadland Photonics, Imacon 792). A framing rate of 50 000 frames s^{-1} was chosen for overview series of the bubble motion at 1.5× original magnification. Framing rates of 1 million and 5 million frames s^{-1} with 2.4-fold enhanced magnification were selected to investigate the final phase of bubble collapse. The exposure

time on the fluorescent screen of the image converter camera is always 1/5 of the interframing time. The image on the fluorescent screen was recorded with a slow scan CCD camera system (Photometrics AT200A) with a 1317×1035 pixel array. The signal from the CCD camera was then digitized with 8-bit resolution (128 grey levels) and passed to a computer. The recorded images show a spatial resolution in object space of 58 μm at a framing rate of 50 000 frames s^{-1} and of 24 μm at 1 million and 5 million frames s^{-1}. Diffuse illumination by a flash lamp through a ground-glass was used to visualize the interior of the bubble. Parallel illumination (without the ground-glass) was used to observe the deformation of the boundary and liquid jet penetration into the boundary. Additionally, the shock waves emitted upon bubble collapse become visible because they deflect the illuminating light out of the imaging lens, changing the brightness of the corresponding region on the photograph (shadowgraph method). To create a three-dimensional impression of its dynamics, the bubble was photographed in side view and also in top view by illuminating the bubble through the PAA sample used as boundary. The triggering of the devices was done electronically with controlled delay times for taking specific sequences out of the overall bubble motion.

2.4. *Determination of bubble size*

For all values of γ, cavitation bubbles of constant size were produced using a constant laser pulse energy of 8 mJ $\pm 3\%$. The resulting bubbles had a maximum radius $R_{max} = 1.55 \pm 0.05$ mm. The bubble size was measured from the picture series for large γ-values taken at 50 000 frames s^{-1}. The value obtained was checked by an indirect measurement using the oscillation time T_{osc} of the bubble at large γ-values. The maximum radius of a spherical bubble situated in a liquid of infinite extent is given by (Rayleigh 1917)

$$R_{max} = \frac{1}{1.83} \left(\frac{p - p_v}{\rho} \right)^{1/2} T_{osc} \tag{2.1}$$

where ρ is the density of the liquid, p the static pressure and p_v the vapour pressure of the liquid. Equation (2.1) assumes that the expansion and collapse phases of the bubble oscillation are symmetric. This condition is fulfilled in the present study, because the bubbles are produced by laser pulses considerably shorter than the bubble oscillation time. The oscillation time of the bubble was obtained by measuring the time interval between the shock waves emitted during optical breakdown and bubble collapse using a fast PVDF hydrophone (Ceram, rise time 12 ns).

R_{max} and the distance s between laser focus and boundary yield the non-dimensional stand-off parameter γ. Note that for $\gamma < 1$ where the expanded bubble is non-spherical, R_{max} represents the radius of a spherical bubble with the same volume (equivalent spherical radius). We assumed that the maximum bubble volume does not change with variation of γ. The equivalent spherical radius is, hence, assumed to be independent of γ for constant laser pulse energy.

3. Results

3.1. *Overview of bubble–boundary interaction*

Figures 3–8 are high-speed photographic records of bubble motion near a PAA boundary with 80% water content which illustrate the essential features of bubble dynamics for different values of the stand-off parameter γ at a framing rate of 50 000

(*a*)

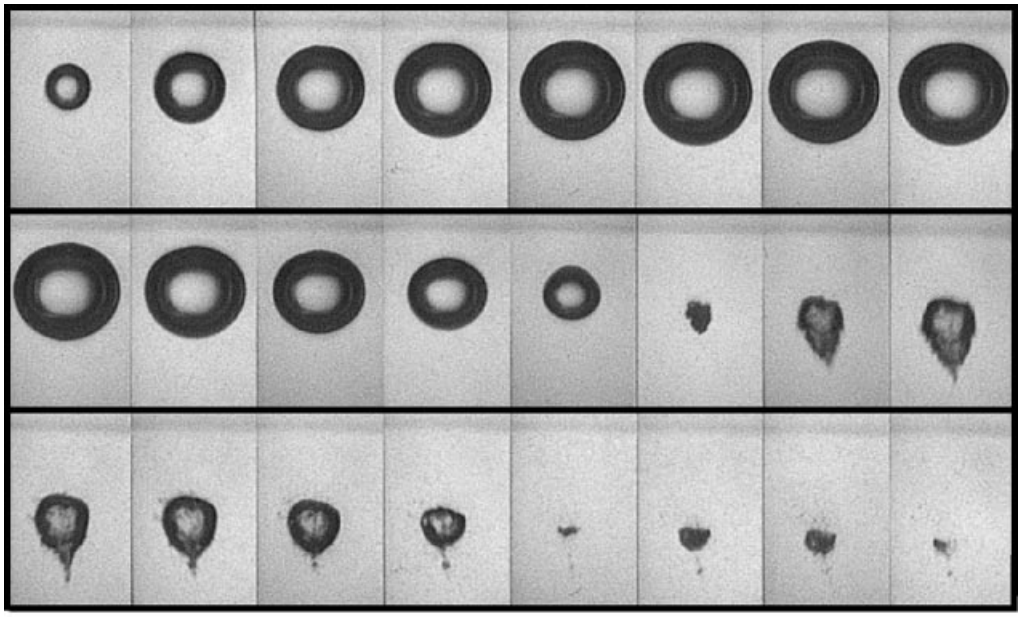

(*b*)

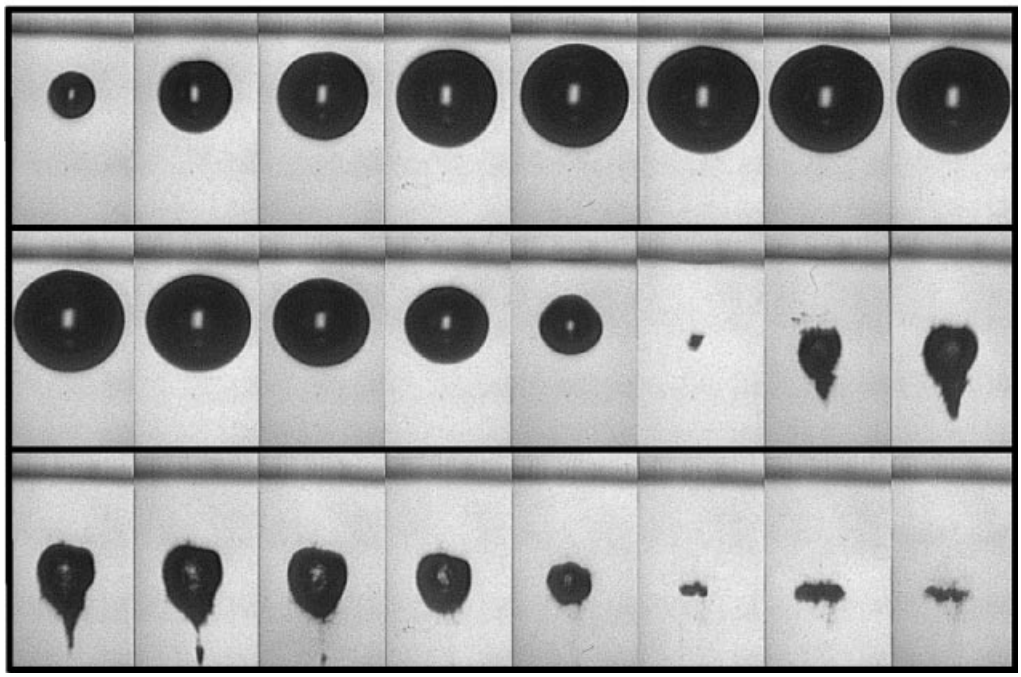

FIGURE 3. Interaction of a laser-produced bubble with an elastic boundary, $\gamma \approx 1.14$. Formation of a liquid jet directed away from the boundary is the main feature of the interaction. (*a*) Side view, diffuse illumination, $\gamma = 1.15$; (*b*) side view, parallel illumination, $\gamma = 1.13$. Frame interval 20 μs. Frame width 3.5 mm.

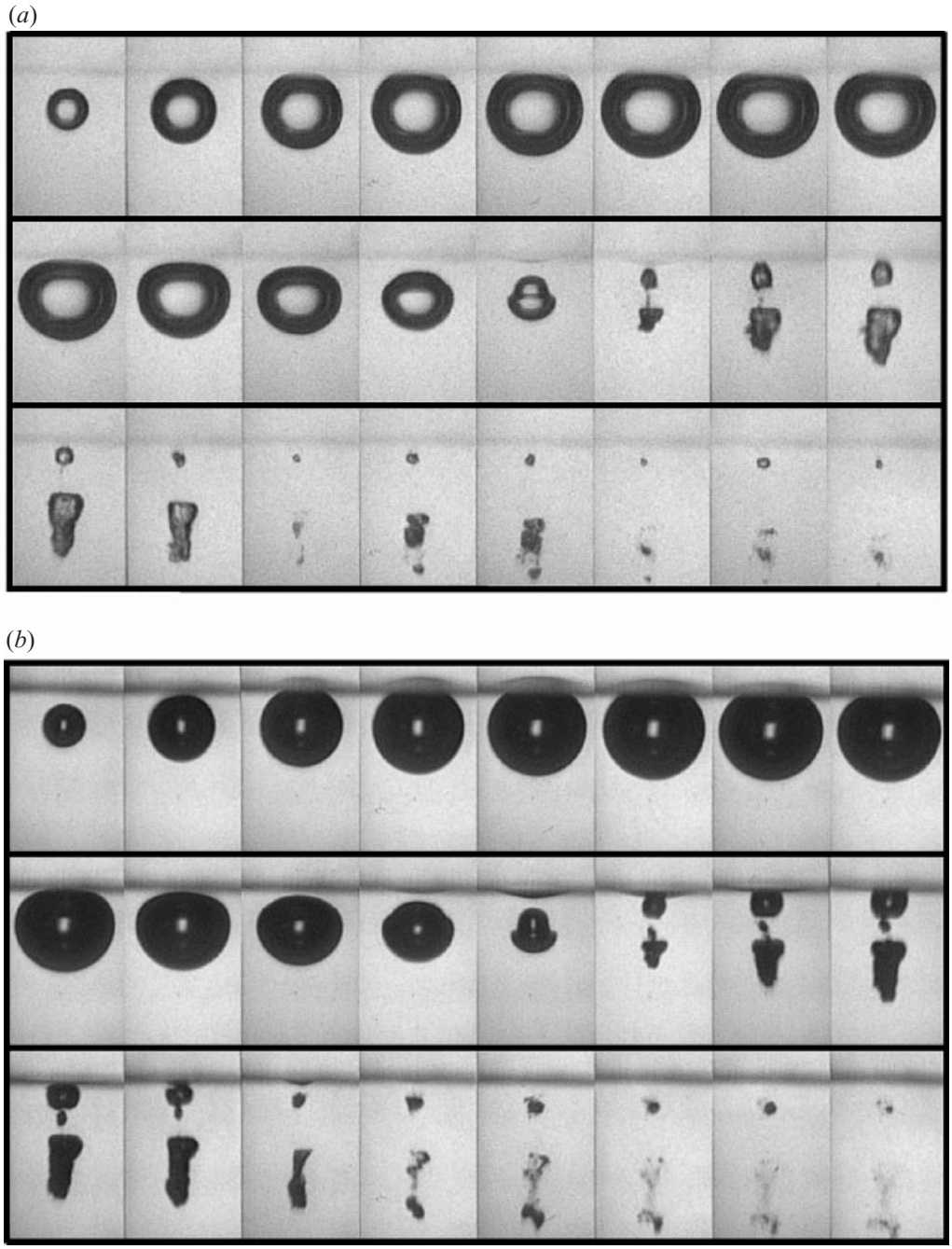

FIGURE 4. Interaction of a laser-produced bubble with an elastic boundary, $\gamma \approx 0.76$. The elastic boundary is compressed during bubble expansion and elevated during bubble collapse. The collapse results in bubble splitting with the formation of two liquid jets in opposite directions. (*a*) Side view, diffuse illumination, $\gamma = 0.77$; (*b*) side view, parallel illumination, $\gamma = 0.75$. Frame interval 20 μs. Frame width 3.5 mm.

(*a*)

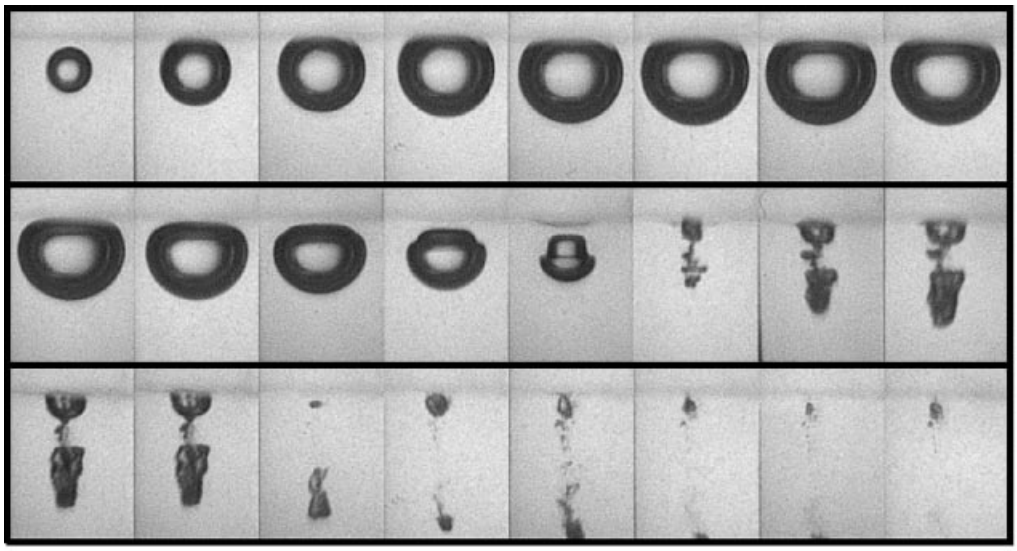

(*b*)

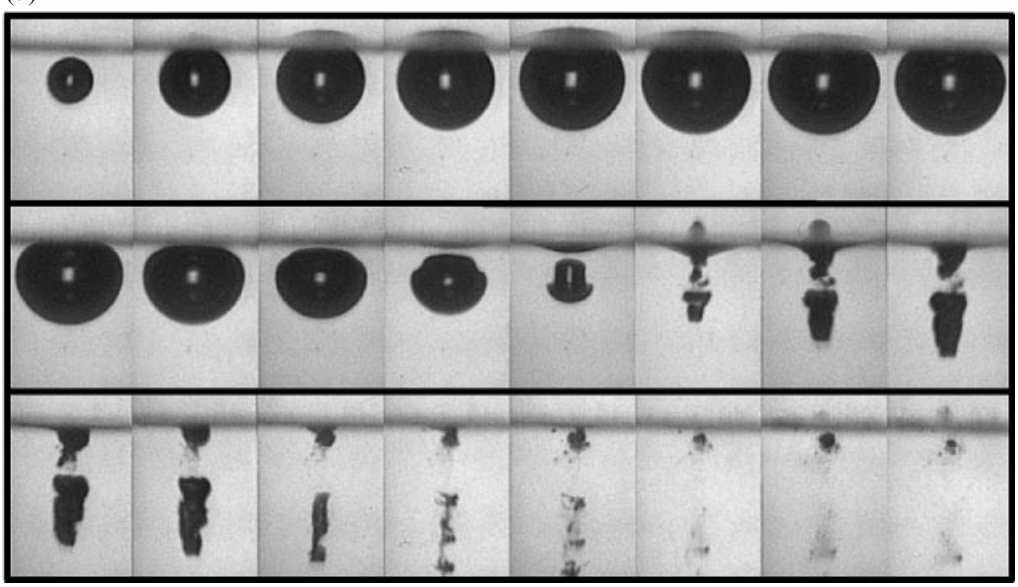

FIGURE 5. Interaction of a laser-produced bubble with an elastic boundary, $\gamma \approx 0.62$. The liquid jet directed towards the boundary penetrates the elastic boundary. (*a*) Side view, diffuse illumination, $\gamma = 0.63$; (*b*) side view, parallel illumination, $\gamma = 0.62$. Frame interval 20 µs. Frame width 3.5 mm.

frames s^{-1}. Part (*a*) of each figure was taken using diffuse illumination, and part (*b*) shows the bubble–boundary interaction with parallel illumination. Both the first and second oscillation period of the bubble are displayed on each photographic sequence. The first frame was taken 5 µs after the moment of optical breakdown. The bubble dynamics near an elastic boundary is mainly oriented in a direction perpendicular to the boundary. To make optimal use of the image format provided by the Imacon camera, the image was rotated by 90° by using a Dove prism inserted in front of the

(*a*)

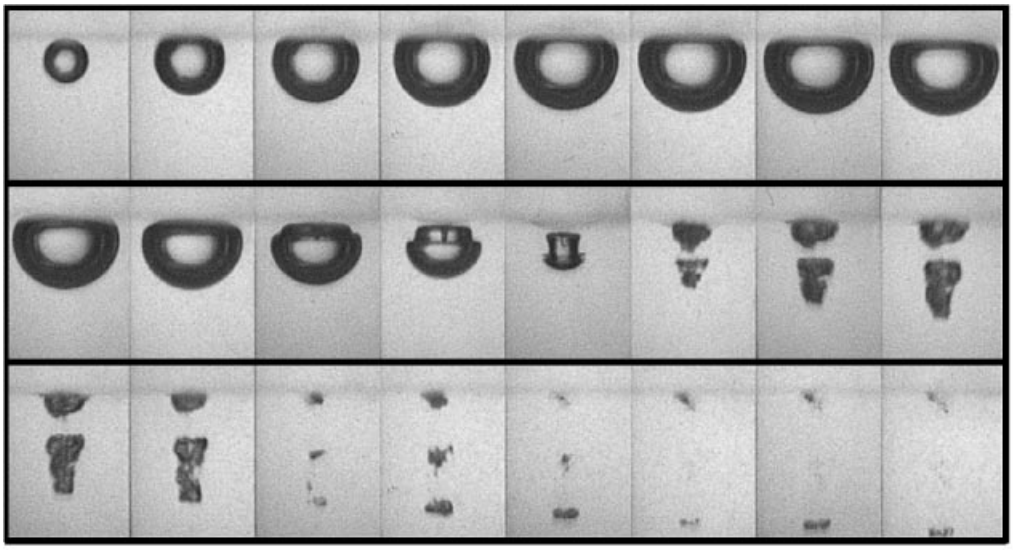

(*b*)

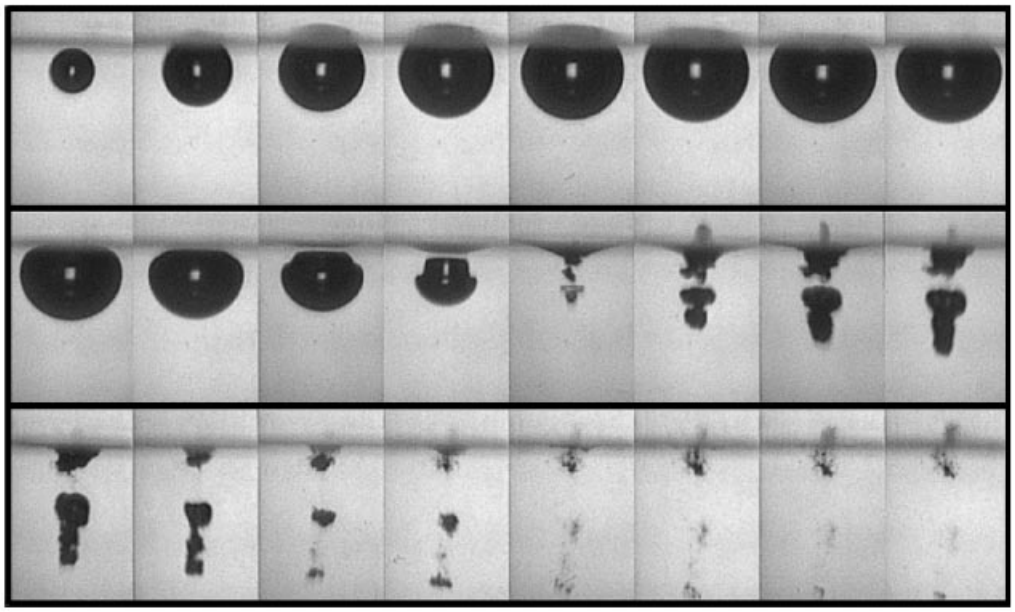

(*c*)

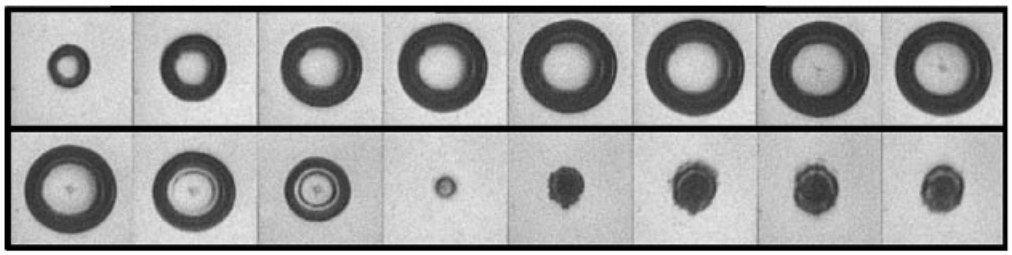

FIGURE 6. For caption see facing page.

camera. Therefore, the elastic boundary is visible in the upper part of the photographic frames when the bubble is photographed in side view.

When the bubble is situated relatively far away from the boundary ($\gamma \approx 1.14$, figure 3), it retains much of its spherical symmetry during expansion and early collapse phases. In the late collapse stage, however, a 'cone-shaped' bubble region develops at the side next to the boundary (frame 13). The collapse of this high-curvature region of the bubble subsequently produces a high-speed axial liquid jet directed away from boundary which leads to the protrusion of the opposite bubble wall. The jet is clearly visible in the bright centre of the bubble images in figure 3(*a*) (frames 15–20). The bubble motion is characterized by a migration away from the boundary, most pronounced during the collapse phases. The photographic sequence taken with parallel illumination shows that the elastic boundary is hardly deformed, except in the final stage of the bubble collapse.

Figure 4 illustrates the bubble behaviour when the value of the stand-off parameter is reduced to $\gamma \approx 0.76$. In this case, the bubble touches the boundary before it reaches the maximum volume. This results in a compression of the elastic boundary during the expansion phase of the bubble with a maximum of the boundary deformation (figure 4*b*, frame 5) occurring before the bubble reaches the maximum size (frame 7). Due to the rebound of the elastic boundary, the bubble becomes flattened in a direction parallel to the boundary. The boundary stays almost motionless for some time and afterwards becomes elevated by the tensile forces exerted during the bubble collapse (figure 4*b*, frames 12–15). Once the oblate shape of the bubble is formed, it collapses from its sides leading to the production of an annular flow which is most pronounced around the surface of the bubble closer to the boundary. Therefore, a mushroom-like shape of the bubble develops in a later stage of the collapse. Additional factors contributing to the formation of the mushroom shape are the low-pressure region between the collapsing cavity and the boundary which holds the bubble wall facing the boundary, and the volcano-like deformation of the boundary, which redirects the inward radial fluid flow along the boundary in a vertical direction. This vertical flow pushes the cap away from the boundary while the collapse proceeds. The annular flow from the bubble sides results in bubble splitting during the final stage of the collapse with the smaller part of the rebounding bubble migrating towards the boundary and the larger part away from the boundary. A liquid jet directed towards the boundary is visible inside the cavity nearest to the boundary while a liquid jet directed away from the boundary can be seen inside the second cavity.

In figure 5, the bubble is created closer to the elastic boundary, corresponding to $\gamma \approx 0.62$. This causes a stronger interaction between bubble and boundary, resulting in a more pronounced flattening of the bubble during the rebound phase of the deformed boundary and the earlier establisment of an annular fluid flow leading to the mushroom-like shape of the bubble. The annular jet leads to bubble splitting into parts of approximately equal size and to the formation of two axial liquid jets in opposite directions which become visible in the rebound phase. The intensity of the liquid jet emanating from the cavity closer to the boundary is, in this case, so high that the jet penetrates the boundary (figure 5*b*, frames 14 and 15). The penetration depth

FIGURE 6. Interaction of a laser-produced bubble with an elastic boundary, $\gamma \approx 0.45$. Jet-like ejection of PAA material occurs during bubble collapse due to the rebound of the deformed boundary. (*a*) Side view, diffuse illumination, $\gamma = 0.45$; (*b*) side view, parallel illumination, $\gamma = 0.44$; (*c*) top view, diffuse illumination, $\gamma = 0.49$. Frame interval 20 μs. Frame width 3.5 mm.

(*a*)

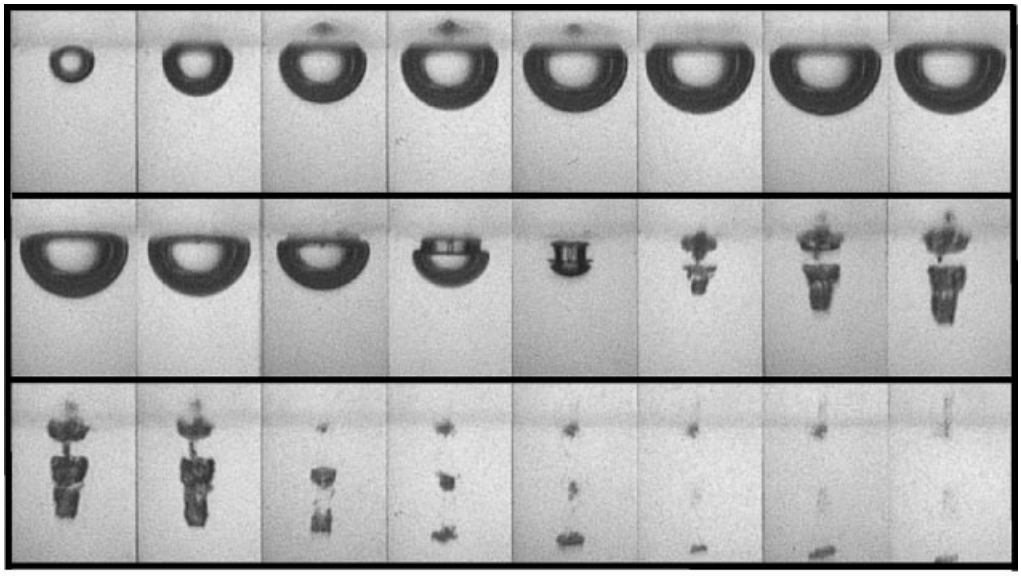

(*b*)

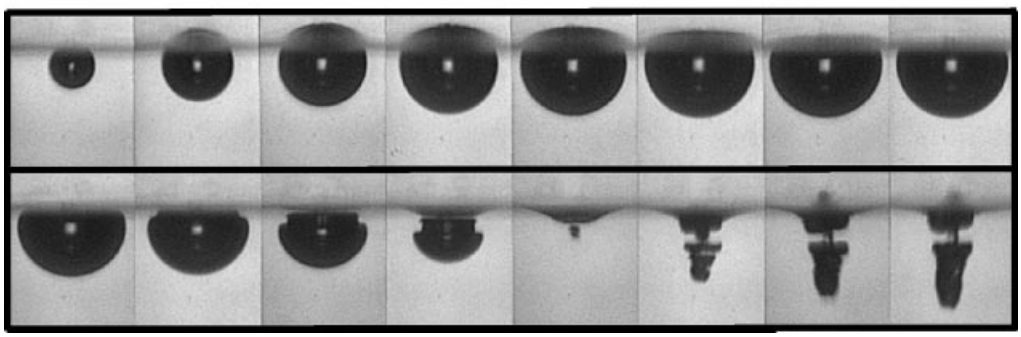

FIGURE 7. Interaction of a laser-produced bubble with an elastic boundary, $\gamma = 0.25$. Both jet-like ejection of boundary material and liquid jet penetration into boundary are observed. (*a*) Side view, diffuse illumination; (*b*) side view, parallel illumination. Frame interval 20 μs. Frame width 3.5 mm.

of this jet into the boundary, measured with respect to the undisturbed surface of the boundary, is 0.53 mm. The damage potential is actually even larger than suggested by this value, because the jet also penetrates the hump formed on the boundary during the late stage of bubble collapse. The total penetration depth of the jet, measured from the peak of the hump, is about 0.9 mm. Liquid jet penetration into the elastic boundary has not been reported in literature. The present experiments employ transparent materials for use as an elastic boundary and thus enable observation of this phenomenon for the first time.

With smaller γ ($\gamma = 0.45$ and $\gamma = 0.25$, figures 6 and 7, respectively), several additional features of the bubble motion attract attention. First, the rebound of the elastically deformed PAA boundary is now accompanied by the formation of a PAA jet which threads the bubble. The PAA jet is visible in the picture series taken with diffuse illumination in side view (figure 6*a*, frames 12 and 13, and figure 7*a*, frames 11–13), and it can be also seen in the pictures series in top view at $\gamma = 0.49$ (figure 6*c*) as a

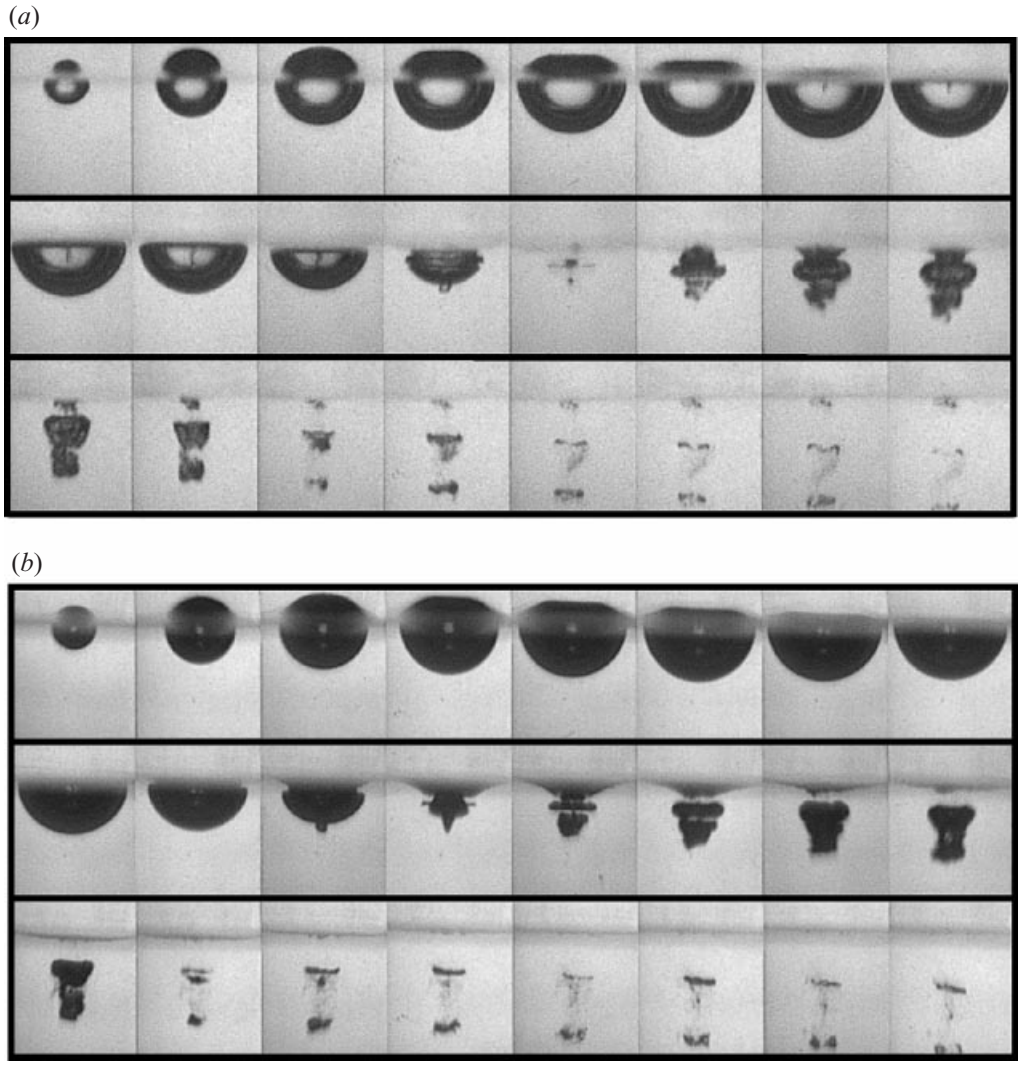

FIGURE 8. Interaction of a laser-produced bubble with an elastic boundary, $\gamma = 0.04$. Strong jet-like ejection of boundary material, formation of a 'volcano-hump' on the boundary during bubble collapse and suppression of liquid jet penetration into the boundary are the main features of the interaction. (*a*) Side view, diffuse illumination; (*b*) side view, parallel illumination. Frame interval 20 µs. Frame width 3.5 mm.

dark spot in the bubble centre (frames 7–12). The top view sequence demonstrates that the PAA jet has already been initiated in a very early stage of the boundary rebound. Its formation is a result of the faster movement of the boundary at the centre of its deformation. In the γ-interval around $\gamma = 0.45$, we also observed bubble–boundary interaction without PAA jet formation as shown in figure 6(*b*). In this sequence taken with parallel illumination the PAA jet would have been visible as a vertical dark bar in the liquid layer between bubble and boundary. The lack of reproducibility of the PAA jet formation causes a similar variability of the liquid jet penetration into the PAA sample. When the PAA jet is not initiated, the liquid jet developed during the collapse of the cavity nearest to the boundary produces a particularly deep penetration into

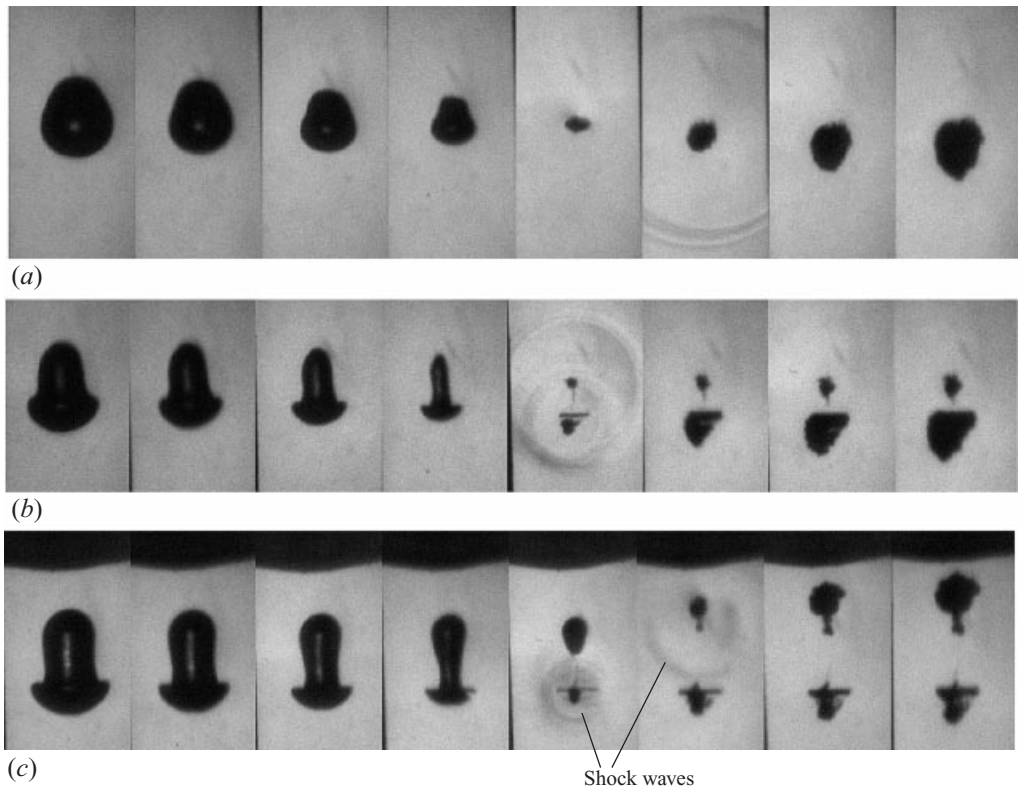

FIGURE 9 (*a–c*). For caption see facing page

the boundary (see also figure 14, below). At $\gamma = 0.25$, both PAA jet formation and liquid jet penetration into the boundary can be observed. The penetration depth is now, however, smaller than that obtained in the absence of the PAA jet, probably, as a result of the collision between these two jets. Another interesting feature observed at $\gamma = 0.45$ as well as at $\gamma = 0.25$ is the appearance of a vortex ring in a very late stage of the collapse, before the splitting of the bubble. It is visible in frame 13 of figures 6(*a*) and 7(*a*). The vortex ring persists during the bubble oscillations after the first collapse, slowly migrating away from the boundary.

Figure 8 shows the case when the bubble is generated almost at the surface of the boundary ($\gamma = 0.04$). Following a strong deformation, the boundary starts to rebound very early during the growth phase of the bubble, and a very strong PAA jet develops which penetrates the bubble wall opposite to the boundary. The maximum height of the PAA jet is about 2 mm. The maximally expanded bubble is no longer an oblate spheroid, as at larger γ-values, but has now an approximately hemispherical shape. The mushroom-like shape of the bubble is not very pronounced, and no bubble splitting occurs. During rebound, the bubble migrates away from the boundary. Consequently, damage of the boundary caused by the penetration of a liquid jet is no longer observed. A volcano-shaped hump develops on the boundary during the final stage of bubble collapse.

3.2. *Bubble collapse and jet formation*

The picture series with 50 000 frames s^{-1} presented above provide a good overview of the variety of phenomena which occur at different stand-off distances between

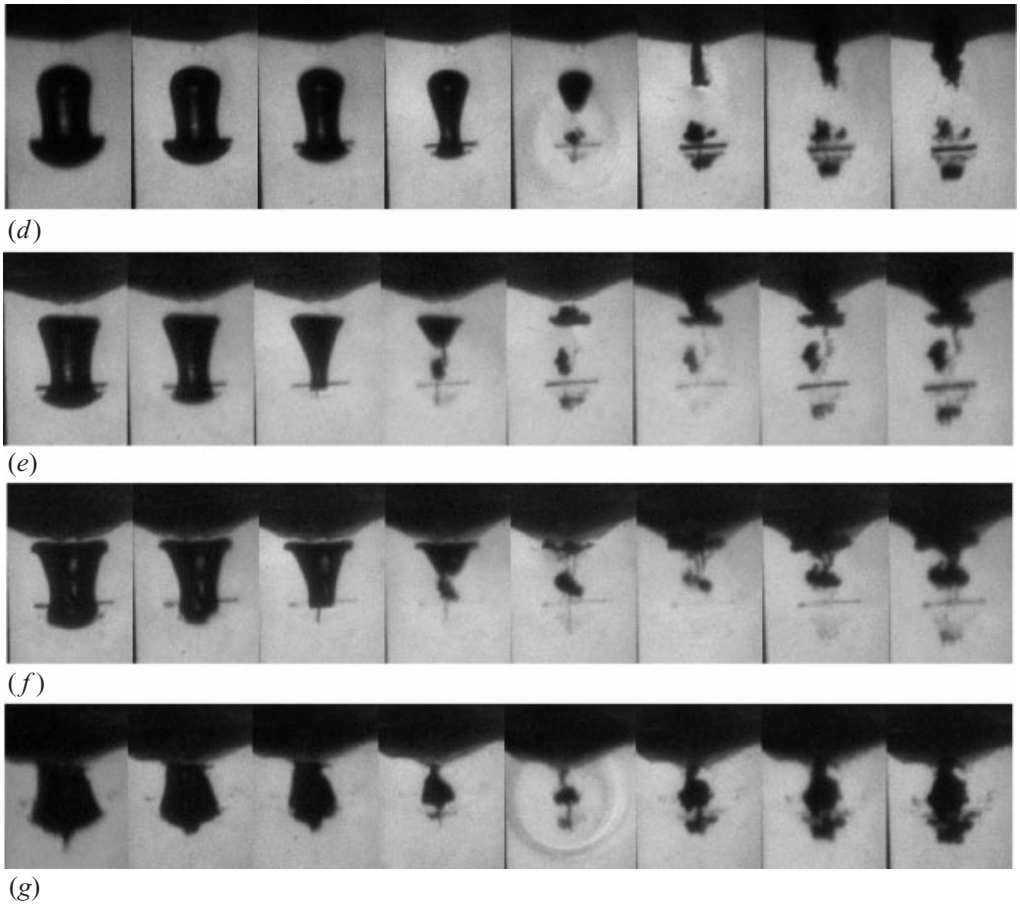

FIGURE 9. Collapse phase of a laser-induced bubble near an elastic boundary. (*a*) $\gamma = 1.13$, (*b*) $\gamma = 0.84$, (*c*) $\gamma = 0.74$, (*d*) $\gamma = 0.6$, (*e*) $\gamma = 0.43$, (*f*) $\gamma = 0.23$ and (*g*) $\gamma = 0.05$. Series taken using parallel illumination with 10^6 frames s^{-1} (frame interval 1 μs). Frame width 1.4 mm.

bubble and boundary. However, the temporal resolution is not sufficient to resolve the final collapse phase where bubble splitting and the formation of axial jets away from or towards the boundary occur. Therefore, figure 9 shows the final stage of bubble collapse for the γ-values presented in figures 3–8 with 1 million frames s^{-1}, i.e. with 20-fold enhanced temporal resolution. In order to visualize the shock waves and the deformation of the boundary, the high-speed photographs are taken using the shadowgraph method with parallel illumination.

At $\gamma = 1.13$ (figure 9*a*), the strongly curved bubble wall facing the boundary collapses faster than the opposite bubble wall, inducing a high-speed liquid jet directed away from the boundary. The jet hits the far bubble wall in the final stage of the collapse and penetrates the bubble during rebound, causing the protrusion on its side far from the boundary. The maximum velocity of this jet, averaged over the interframing time of 1 μs, is 380 m s^{-1}. Two shock waves are emitted during bubble rebound (frame 6). The first wave (the shock wave with the larger diameter) is probably created by the impact of the high-speed liquid jet onto the opposite bubble wall, and the second one as a consequence of the strong compression of the bubble content at its minimum volume (Ohl, Philipp & Lauterborn 1995).

At $\gamma = 0.84$ (figure 9*b*), the bubble assumes a mushroom-like shape during collapse. The annular fluid flow parallel to the boundary is fast, but the flow from the side of the boundary is inhibited. Therefore, the foot of the mushroom collapses more strongly from the sides, resulting in bubble splitting. Two sets of shock waves can be seen after splitting (frame 5) each of them interacting with the other cavity. The position of the shock waves centre and their diameter indicates that the small cavity nearest to the boundary collapses first. When the resulting shock wave hits the larger bubble, it contributes to the formation of a jet directed away from the boundary.

At $\gamma = 0.74$ (figure 9*c*), the cylindrical part of the cavity necks during the final stage of bubble collapse as a result of the annular liquid flow induced in an earlier stage of the collapse. At closure of the neck, the bubble splits in two. The cavity situated far away from the boundary now collapses first and its collapse is accompanied by liquid jet formation directed away from the boundary. The cavity nearest to the boundary acquires an almost triangular shape subsequent to the bubble splitting and is then hit by the shock waves emitted during the rebound of the other cavity. It therefore collapses with a high-speed liquid jet and a strong translational motion directed towards the boundary. Whereas the maximum velocity of the liquid jet directed towards the boundary is $710\,\mathrm{m\,s^{-1}}$, only $325\,\mathrm{m\,s^{-1}}$ was measured for the jet directed away from the boundary. The translational motion of the cavity nearest to the boundary is larger than that of the cavity far away from the boundary so that the migration of the two-bubble system can be considered as directed towards the boundary. Since at $\gamma = 0.84$ the migration of the two-bubble system is directed away from the boundary we conclude that the neutral bubble collapse, where the centre of gravity of the two-bubble system maintains its initial position, occurs between $\gamma = 0.74$ and $\gamma = 0.84$.

When the value of the stand-off parameter is reduced to 0.6 (figure 9*d*), the behaviour is similar as in figure 9(*c*), but the liquid jet movement towards the boundary is even faster. By frame 5 the shock wave has passed over the cavity situated nearest to the boundary, and a high-speed liquid jet is initiated which crosses the cavity and, 1 μs later, impacts the boundary. The maximum velocity of this jet is $810\,\mathrm{m\,s^{-1}}$. Even this value represents a lower estimate of the jet velocity because the exact position of the jet tip cannot be precisely determined in frame 6; it is likely that the jet tip has already penetrated into the boundary. In figure 9(*d*) one can also follow nicely the formation of the vortex ring which is observed in the late stages of the bubble collapse and during rebound for $\gamma \leqslant 0.74$ (see also figures 5–8). The vortex ring arises when the upward flow along the necked shape of the mushroom stem, induced by the deformation of the boundary towards the bubble, meets the inward motion of the liquid, induced by the collapsing cap of the mushroom. The upward flow along the mushroom stem results in the separation of a portion of the cap base when the angle between stem and cap exceeds 90° (frames 3 and 4).

With smaller γ, some changes are observed in the bubble behaviour. At $\gamma = 0.43$ (figure 9*e*) no shock wave is emitted by the cavity oscillating far from the boundary. The reason for the absence of a shock wave is that the cap of the mushroom-like shape of the bubble ends its collapse before the splitting phenomenon has occurred. The minimum volume of the mushroom cap is reached in the third frame of the photographic sequence, i.e. 1 μs before the bubble splitting. Consequently, the gas and vapour content of the cap is not compressed during its collapse but pushed into the larger volume of the rest of the bubble (mushroom foot). The pressure rise inside the collapsing cap and in the region of the bubble neck is, therefore, relatively low during the whole collapse period, resulting in a weaker force driving the liquid jet towards

FIGURE 10. Jet-like ejection of boundary material during bubble collapse near an elastic boundary, $\gamma = 0.1$. The photographic sequence is taken by using diffuse illumination with 10^6 frames s^{-1} (frame interval 1 μs). Frame width 1.4 mm.

the boundary. The jet is, furthermore, counteracted by the formation of a PAA jet during the collapse phase of the bubble.

At $\gamma = 0.23$ (figure 9*f*), the PAA jet causes the protrusion of the mushroom cap visible in the second frame of the series, and it becomes directly visible during the rebound phase of the bubble as a vertical structure with dark edges (frames 5–8). The liquid jet directed towards the boundary is certainly strongly decelerated by the PAA jet. Nevertheless, it is still capable of penetrating the boundary (see figure 7) because the liquid layer between bubble and boundary is now very thin.

At $\gamma = 0.05$ (figure 9*g*), the annular liquid flow parallel to the boundary is apparently strongest near the PAA surface. Therefore, the bubble collapses fastest at the side adjacent to the boundary, no bubble splitting occurs, and no liquid jet towards the boundary is formed. The PAA jet is very strong and it may be supported by a weak liquid flow away from the boundary. The PAA jet is visible as protrusion of the mushroom cap (see also figure 8). The collapse of the mushroom cap around the PAA jet results in the emission of a shock wave which is visible in frame 5. Interestingly the bubble collapses fastest at the side closer to the boundary both for large and for very small γ-values. In the former case, this is a consequence of the strong flow component from the side of the boundary, whereas in the latter case the flow is initially more equatorial.

The PAA jet inside the collapsing bubble is illustrated in the photographic sequence of figure 10 which was taken with diffuse illumination at $\gamma = 0.1$. The diameter of the PAA jet is about 140 mm.

Figure 11 shows the maximum velocity of the liquid jets directed towards and away from the elastic boundary as a function of the stand-off parameter γ. The values of the jet velocity are derived from the framing series taken with 1 million frames s^{-1}. The maximum velocities reached by both jets are strikingly high: velocities of up to 800 m s^{-1} were measured for the liquid jet directed towards the boundary at a γ-value around 0.6. The jet velocity becomes smaller when γ is reduced so that at $\gamma = 0.1$ the maximum jet velocity is about 200 m s^{-1}. The maximum velocity of the liquid jet directed away from the boundary is, on the other hand, nearly constant in the parameter range $1 \leqslant \gamma \leqslant 2.5$, at a value of about 400 m s^{-1}. A significant influence of the stand-off parameter is observed only for $\gamma < 1$ where the velocity decreases to about 200 m s^{-1} at $\gamma = 0.6$.

3.3. *Jet formation in the bubble splitting domain*

The fastest sequence of events takes place in the range of γ-values where bubble splitting occurs. It is here that the velocity of the axial liquid jets reaches very high values and the shock waves emitted during the bubble rebound have the largest amplitude. To get a clearer picture of the formation of the high-speed jets we have investigated the final phase of bubble collapse in this γ-interval using 5 million

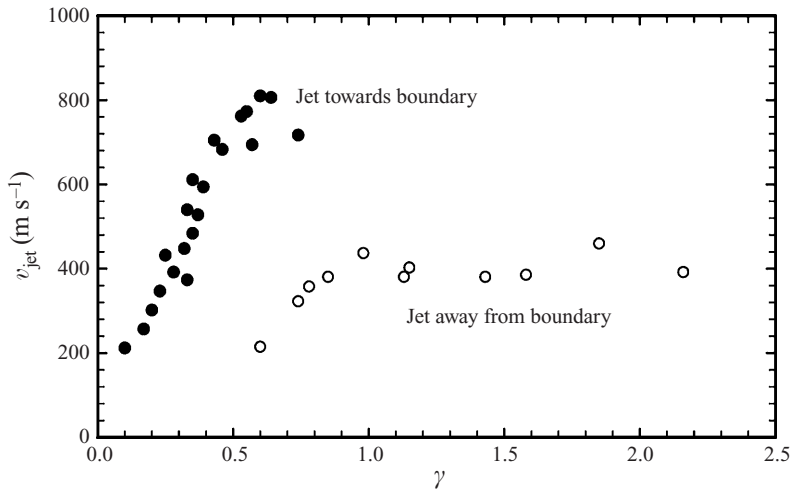

FIGURE 11. Maximum velocities of the liquid jets directed towards the elastic boundary (filled symbols) and away from the boundary (open symbols). The values of the jet velocity are determined from photographic series taken with 10^6 frames s^{-1}.

frames s^{-1}. The results are illustrated in the collection of photographic sequences shown in figure 12 where γ ranges from 0.91 to 0.6. The images of the shock waves emitted upon bubble collapse are sharper at this framing rate because of the relatively short exposure time of 40 ns. Analysis of the distances travelled by the individual shock waves at the time of exposure allows one to deduce the bubble dynamics with an even better time resolution than that given by the interframing time.

With decreasing γ, the location where the bubble first collapses moves from the bubble side nearest to the boundary to its side far from the boundary. This process is coupled with a reversal in the direction of the main flow of the axial jets. The main jet is directed away from the boundary at large γ-values when the bubble side nearest to the boundary collapses first, and directed towards the boundary when the far bubble side collapses first. At $\gamma = 0.91$ (figure 12*a*), the foot collapses first with a travelling collapse wave starting from the boundary side (frame 2) which induces a high-speed liquid jet directed away from the boundary. At a slightly smaller γ-value ($\gamma = 0.86$, figure 12*b*), the collapse is nearly synchronous along the whole length of the foot but now starts from the necked section induced by the annular jet (frame 2). Then the foot part near the boundary collapses, followed by the cap. For $\gamma = 0.81$ (figure 12*c*) and $\gamma = 0.74$ (figure 12*d*), the collapse starts from the necked section as in the previous case of $\gamma = 0.86$. However, it now leads to bubble splitting, followed by the collapse of the cap and, afterwards, the foot. At $\gamma = 0.74$, the two shock waves emitted upon the collapse of the neck and of the cavity far from the boundary both drive the collapse of the cavity closer to the boundary (frames 3 and 4) thus producing a high-velocity jet towards the boundary. The action of the shock waves redirects the liquid flow from the annular jet formed earlier during the bubble collapse. In this way the fluid is focused from a very large solid angle into an axial jet. At the slightly larger γ-value of 0.81, jet formation towards the boundary is not yet observed because the portion of the bubble close to the boundary is so small that its shock-wave-driven collapse does not lead to the focusing of a considerable amount of liquid. At the smaller value of $\gamma = 0.6$ (figure 12*e*), the foot of the mushroom-shaped bubble is,

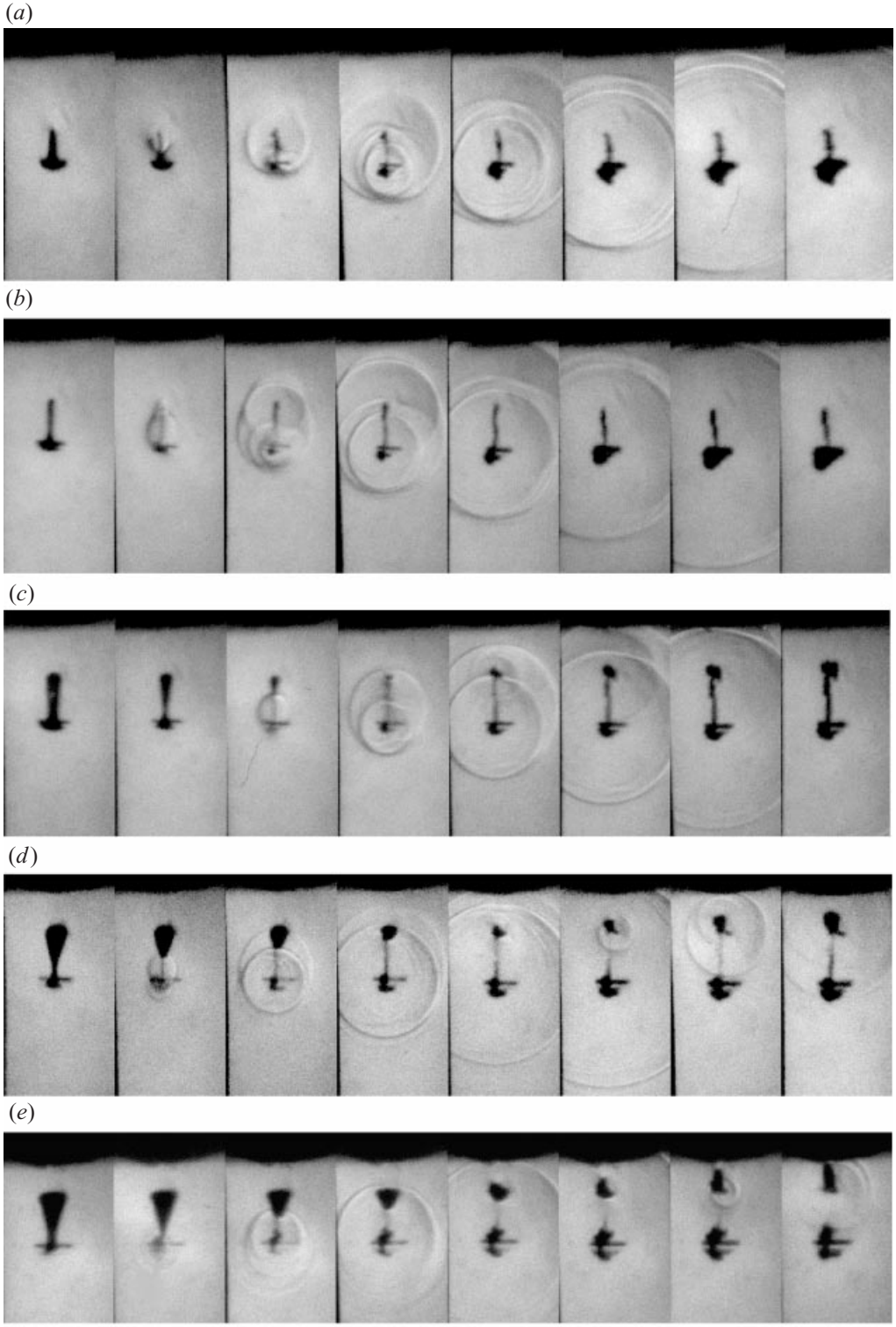

FIGURE 12. Final phase of the bubble collapse near an elastic boundary. (*a*) $\gamma = 0.91$, (*b*) $\gamma = 0.86$, (*c*) $\gamma = 0.81$, (*d*) $\gamma = 0.74$ and (*e*) $\gamma = 0.6$. Series taken with 5×10^6 frames s^{-1} (frame interval 200 ns). Frame width 1.4 mm.

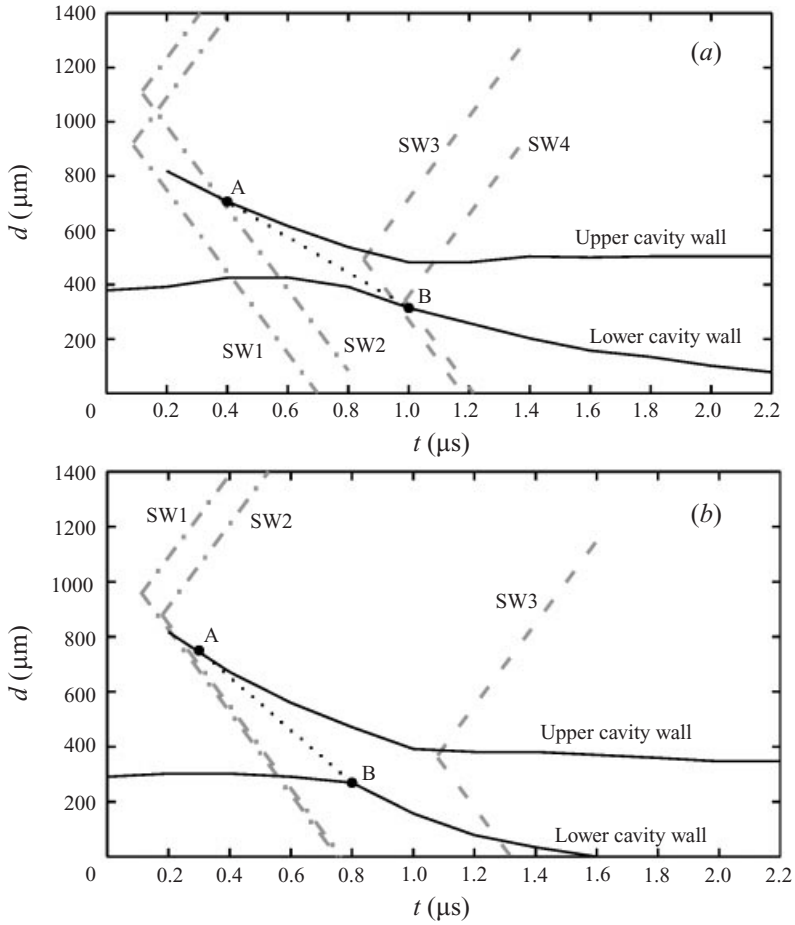

FIGURE 13. Temporal development of the positions of the upper and lower walls of the cavity closer to the elastic boundary formed after bubble splitting. (*a*) $\gamma = 0.74$, (*b*) $\gamma = 0.6$. The dash-dotted lines denote the position of the shock waves emitted upon bubble collapse while the dashed lines denote the shock waves emitted during the cavity rebound. Further explanations are given in the text.

in contrast, significantly larger than the cap. The cap and the neck collapse almost synchronously. The shock-wave-driven collapse wave travelling from the cap towards the foot is therefore particularly strong, and because of the conical shape of the foot it continues to focus fluid from the annular flow into an axial jet until it reaches the base of the foot (Birkhoff *et al.* 1948). This process leads to the formation of a very high-velocity liquid jet which penetrates the boundary (frame 8) even though the boundary is protected by a water layer of 0.35 mm thickness.

To assist in the interpretation of the origin of the high-velocity jet directed towards the boundary we have plotted in figure 13 the relative positions of the upper and lower walls of the cavity closer to the boundary versus time for $\gamma = 0.74$ and $\gamma = 0.6$, together with the shock wave propagation. The results were obtained from high-speed photographic series taken with 5 million frames s^{-1}. The initial part of the plots corresponds to the photographic sequences shown in figure 12(*d*) ($\gamma = 0.74$) and figure 12(*e*) ($\gamma = 0.6$); the data at later times were obtained from frames not shown in the figures. The dash-dotted lines denote the position of the shock waves emitted

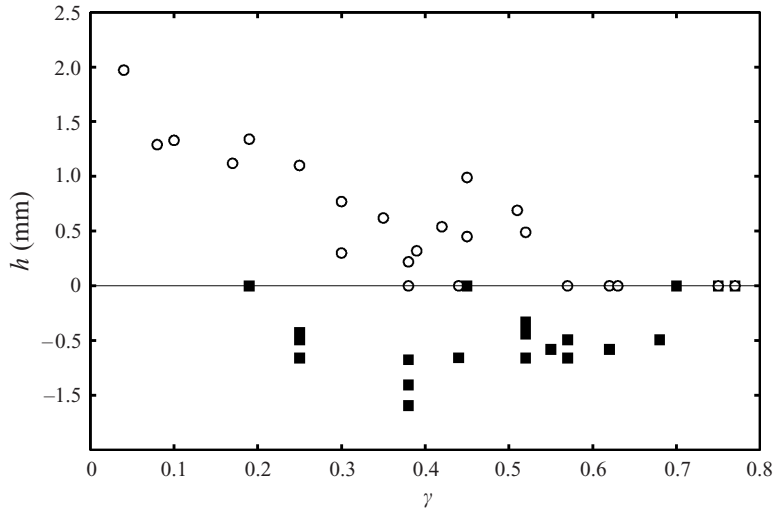

FIGURE 14. Penetration depth of the liquid jet into the PAA sample (filled symbols) and height of the PAA jet (open symbols). Both values are measured with respect to the undisturbed surface of the elastic boundary.

upon bubble collapse while the dashed lines denote the shock waves emitted during the cavity rebound. The shock wave centres were estimated from the position of the acoustic transients on the photographic frames using the normal velocity of sound in water (1490 m s^{-1}). The exact velocity of the acoustic transients is, most likely, higher in the initial stage of the propagation, but probably only for less than 200 ns (Vogel *et al.* 1996*a*). We have considered the flattening of the cavity wall furthermost away from the boundary as the beginning of jet formation (point A). This perturbation of the cavity wall is induced by the impact of the shock waves emitted upon the collapse of the neck (SW1 at $\gamma = 0.74$ and SW2 at $\gamma = 0.6$) and cap (SW2 at $\gamma = 0.74$ and SW1 at $\gamma = 0.6$) of the mushroom-shaped bubble. The jet then crosses the cavity and penetrates the opposite wall of the cavity (point B) which, until then, is almost motionless. Shock waves are emitted by the impact of the liquid jet onto the cavity wall facing the boundary (SW4) and at the minimum volume of the cavity (SW3). At $\gamma = 0.74$, the jet tip hits the opposite cavity wall after the cavity reaches its minimum volume and the high pressure developed within the cavity probably acts to retard the jet motion. The maximum jet velocity, averaged over the time between points A and B (600 ns), is $v_{max} = 654$ m s^{-1}. The jet is strongly decelerated on its way to the boundary by the water layer between cavity and boundary (≈ 0.45 mm in thickness) and, for the time interval shown here, there is no impact of the jet onto the boundary. By 1.6 µs after the shock impingement onto the upstream wall of the cavity, the jet velocity has decreased to 95 m s^{-1}. Examination of high-speed photographic sequences covering later times showed that the impact velocity of the jet onto the boundary is as small as 10 m s^{-1}. The production of jet-induced damage of the boundary is therefore unlikely at this γ-value (see also figure 4 where no damage of the PAA sample is observed). In contrast, at $\gamma = 0.6$, the jet tip collides with the opposite cavity wall some time before the bubble reaches its minimum volume. The jet is continuously accelerated until the very last moment before the collision, resulting in an exceptionally high value of its velocity. The maximum jet velocity, averaged over the time between points A and B (700 ns), is in this case $v_{max} = 960$ m s^{-1}. That is the largest value measured in

the present investigations. As the water layer between bubble and elastic boundary decelerates the jet, the impact velocity at the boundary (170 m s^{-1}) is again smaller than v_{max}. It is, however, high enough to produce the jet penetration into the PAA sample visible in figure 5.

3.4. *Cavitation erosion*

The penetration depth of the liquid jet into the boundary and the maximum height of the PAA jet are shown in figure 14 as a function of the stand-off parameter γ. The PAA jet was observed for $\gamma \leqslant 0.52$ and its maximum height increases with decreasing γ. The PAA jet formation is not very reproducible for $0.3 < \gamma < 0.52$, probably because the stress driving this jet is close to the plastic flow stress of the PAA material. Liquid jet penetration into the boundary was observed in the range $\gamma = 0.25$ to 0.68. This implies that for this range of γ the impact velocity of the jet onto the boundary generates a water hammer pressure higher than the plastic flow stress of the boundary. The maximum penetration depth of 1.1 mm was reached at $\gamma = 0.38$, in a case where no PAA jet was initiated.

4. Discussion

The interaction between laser-induced cavitation bubbles and flexible boundaries is highly complex and includes annular jets leading to bubble splitting, liquid jet formation towards and away from the boundary, and material ejection into the liquid. The highest value of the jet velocity measured was 960 m s^{-1}, that is about six times as fast as the highest jet velocities observed near rigid boundaries (150 m s^{-1}, Brujan *et al.* 2001; Vogel, Lauterborn & Timm 1989). To better understand the complex behaviour and the origin of the fast jets, it is helpful to first analyse the principal mechanisms involved in the various kinds of jet formation. As a second step, we can then discuss the mutual interaction of these mechanisms to analyse the parameter dependence of the bubble dynamics.

4.1. *Axial and annular jets*

A jet develops if one part of the bubble collapses faster than the other parts. Slight differences in the collapse velocity are amplified during bubble collapse by geometrical 'focusing' of the asymmetric flow. When one or both poles of the bubble collapse faster than the other parts, needle-like jets develop. When the equatorial region collapses faster, an annular, disk-like flow towards the bubble centre develops which leads to bubble splitting and to the formation of two needle-like jets flowing in opposite directions perpendicular to the equatorial plane. The type of jet formation that occurs or dominates depends on the initial bubble shape and on the boundary conditions.

Under symmetric boundary conditions (static fluid, no buoyancy), jet formation arises when the bubble shape is aspherical. A bubble having the form of a prolate spheroid develops two 'axial' jets directed towards the centre (Chapman & Plesset 1972; Godwin *et al.* 1999). An oblate spheroid develops an 'annular' jet (Chapman & Plesset 1972). When the fluid rushing in from the bubble equator meets in the bubble centre, the bubble splits in two parts and two jets flowing in opposite directions towards the poles develop (Lauterborn & Hentschel 1985; Blake *et al.* 1997*a*). In both cases the jets originate from those parts of the bubble wall which have the largest curvature. Lauterborn (1982) and Godwin *et al.* (1999) showed that the proportional relationship between the radius of a spherical bubble and collapse time (Rayleigh 1917) may be adopted for the local radii of a non-spherical bubble as well.

A large curvature corresponds to a small bubble radius and thus leads to a short 'local' collapse time.

When the bubble oscillates under asymmetric boundary conditions, it is usually exposed to pressure gradients. This leads to a faster collapse of the bubble section(s) exposed to a higher pressure, and to jet formation even for an initially spherical bubble. Which type of jet forms depends on the complexity of the boundary conditions. In simple cases when there is only one force acting on the bubble, an axial jet is formed. In more complex situations, when opposing effects act on the bubble motion, an annular jet can be formed if the strength of both effects is approximately equal. Examples of axial jets from unidirectional pressure gradients are:

(i) Jet through a buoyant bubble. The jet forms because of the hydrostatic pressure difference between lower and upper bubble walls (Benjamin & Ellis 1966).

(ii) Jet formed when a shock wave hits a gas bubble (Birkhoff *et al.* 1948; Bowden 1966; Dear, Field & Walton 1988; Philipp *et al.* 1993).

When buoyancy forces can be neglected (i.e. for small bubbles with short oscillation times), further examples for axial jet formation are:

(iii) Jet towards a flat rigid wall. The pressure gradient causing the jet formation is due to the low-pressure region between bubble and wall developing during bubble collapse (Benjamin & Ellis 1966; Plesset & Chapman 1971; Blake, Taib & Doherty 1986; Vogel *et al.* 1989; Philipp & Lauterborn 1998). During the initial collapse phase, the bubble acquires the form of a prolate spheroid. This shape also contributes to the formation of the axial jet.

(iv) Jet away from a free surface caused by the high-pressure region developing between bubble and surface during the expansion phase (Blake, Taib & Doherty 1987; Blake *et al.* 1997*a*).

Examples of annular jets arising from pressure gradients oriented in opposite directions are:

(i) Bubble between two rigid walls (Chahine 1982).

(ii) Buoyant bubble above a plate, or below a free surface (Blake *et al.* 1986, 1997*a*).

(iii) Bubble in an axisymmetric stagnation flow towards a rigid wall. The stagnation flow creates a stationary pressure gradient directed away from the wall, and the bubble oscillation in the vicinity of the wall is associated with a time-dependent gradient directed towards the wall (Robinson & Blake 1994; Blake *et al.* 1997*a*). Due to the stagnation flow, the expanding bubble is deformed into an oblate spheroid. This shape initiates the formation of an annular jet (Chapman & Plesset 1972; Voinov & Voinov 1976) which is further accelerated by a ring-shaped region of high pressure surrounding the bubble that develops when the bubble walls are already indented (Robinson & Blake 1994).

(iv) Bubble between a flat rigid wall and another bubble (Blake *et al.* 1993; Tomita, Sato & Shima 1994). Besides the pressure gradient directed towards the wall, the bubble is subjected to a time-dependent pressure gradient directed away from the wall induced by the low-pressure region between the two bubbles.

(v) The bubble dynamics near elastic, deformable boundaries also belongs to the class of jet formation in the presence of opposite pressure gradients. As in the case of the rigid wall, the bubble oscillation in the vicinity of the wall is associated with a time-dependent pressure gradient directed towards the wall. Unlike the rigid wall, however, the material is now deformed during bubble expansion, it rebounds, and thus creates a time-dependent flow and pressure gradient directed away from the wall (Gibson & Blake 1982; Shaw *et al.* 1999; Kodama & Tomita 2000).

When the opposite forces are not equally strong, the bubble splits into unequal parts, and the jet originating from the larger bubble part is stronger than the other jet in the opposite direction. The velocity of the dominating needle-like jet becomes very high, because the region from which the fluid flow is focused into the jet is large, and the jet has a small diameter (Voinov & Voinov 1976; Robinson & Blake 1994; Blake *et al.* 1997*a*). In the limit, however, where one force is much stronger than the other, only one axial jet is formed which is relatively thick and slow (Voinov & Voinov 1976).

4.2. *Jet formation and bubble splitting near the elastic PAA sample*

For large γ-values, we observed an axial jet flow directed away from the boundary (figure 3). This indicates, according to the above analysis, that the flow induced by the rebounding PAA sample is stronger than the Bjerknes attractive force caused by the low pressure between bubble and boundary which develops during the late stage of the collapse phase.

With decreasing γ-value, due to a strong pressure decrease in the liquid layer between bubble and boundary, the strength of the Bjerknes force increases faster than the flow from the boundary, resulting in a more equal magnitude of the opposing forces. Therefore, an annular jet develops which leads to bubble splitting and the formation of two axial jets in opposite directions (figures 4–7). The deformability and rebound of the elastic material allows the formation of an oblate spheroidal bubble shape even when the bubble is produced at a small distance from the boundary. The oblate spheroidal shape is essential for the formation of the annular jet flow. The strongest convex curvature and thus the highest collapse velocity are at first found near the bubble equator. The fast collapse of these bubble parts is the driving force for the annular jet. The fast equatorial flow results in a ring-shaped indentation of the bubble wall and probably in the generation of a ring-shaped region of high pressure (Robinson & Blake 1994) which further accelerates the annular jet.

For very small γ-values, the PAA surface is strongly deformed upon bubble expansion, and therefore a strong PAA jet develops early during the collapse phase. The maximally expanded bubble has now an approximately hemispherical shape (figure 8), and the fastest flow is observed directly at the PAA surface (figure 9*d*). Therefore, no annular jet is formed and no bubble splitting occurs. During the final collapse phase, when the volcano-like hump is formed at the PAA surface, the annular flow is transformed into an axial flow away from the boundary and the bubble starts to move away from the PAA surface. This process together with the PAA jet prevents the formation of a liquid jet penetrating the PAA sample.

The dynamics of annular jet formation at intermediate γ-values is first influenced by the upward directed flow from the rebounding surface and then by the low-pressure region between bubble and boundary which 'holds' the lower bubble wall and lifts the surface of the PAA material. This sequence of 'push and hold' probably creates the characteristic mushroom-like bubble shape observed during collapse in most of the cases shown. The flow created by the upward motion of the elastic wall collides with the flow parallel to the surface induced by the bubble collapse. In the end phase of the collapse, when the surface has formed a hump below the bubble, part of the horizontal flow is also deviated by the hump in the upward direction. This flow pattern probably leads to the indentation of the bubble wall at the transition between mushroom foot and cap and it probably also explains why this indentation moves rapidly upward during the late collapse phase. A bubble with a mushroom-like shape is also developed when a buoyant bubble collapses above a flat rigid boundary

in a forward stagnation-point flow (Blake *et al.* 1986). The movement of the liquid in the mushroom neck resembles the 'splash' developing under certain conditions during the bubble collapse near a solid wall (Tong *et al.* 1999; Blake, Tomita & Tong 1997*b*).

The bubble splitting process and the subsequent formation of needle-like jets along the vertical bubble axis are caused by the annular jet flow, but they are also influenced by the upward flow originating from the rebounding PAA surface. The climbing of the mushroom neck during the bubble collapse shifts the location where the bubble splits further away from the boundary. The redirection of the annular jet flow into axial jets is mediated by the shock waves from the mushroom 'foot' or 'cap', respectively. Only in a very small γ-interval does the 'neck' collapse first, and both axial jets are approximately symmetric. In most cases, the collapse is asymmetric and one axial jet dominates.

The highest jet velocity is achieved for γ-values around $\gamma = 0.65$, where an asymmetric annular jet leads to the formation of a strong axial jet towards the elastic boundary. Various factors contribute to the high jet velocity of up to $960\,\mathrm{m\,s^{-1}}$:

(i) The fluid flow is focused from a very large solid angle into a very thin jet. The solid angle from which the jet flow originates is probably larger than in the case of a rigid boundary. Moreover, the resulting jet is considerably thinner, because the redirection of the annular flow into axial jets occurs in a very late collapse stage.

(ii) The driving pressure is larger than in the case of a rigid boundary. The jet flow near a rigid boundary is, in the final collapse stage, driven by the pressure from a stagnation point above the bubble (Blake & Gibson 1987). In the case of an elastic boundary at $\gamma \approx 0.65$, the annular jet is accelerated by a pressure ring, and the redirection into an axial jet is mediated by the shock waves emitted upon the collapse of the mushroom cap and neck (see figure 12*d*, *e*).

(iii) The jet is not only redirected by the shock wave but also further accelerated, because the bubble part next to the boundary has a conical shape which allows a continuous shock-wave-driven focusing of the annular flow into the axial jet until it reaches the opposite bubble wall (Birkhoff *et al.* 1948).

4.3. *Kelvin impulse*

The concept of the Kelvin impulse was applied to bubble dynamics by Benjamin & Ellis (1966) to explain the acceleration of a translating cavity during its collapse, which is coupled with the formation of a jet and the transformation of the bubble into a hollow vortex ring. When the bubble is exposed to a pressure gradient, a Bjerknes force is created leading to a translation of the bubble with respect to the surrounding liquid. The Kelvin impulse can be interpreted as a linear impulse of the bubble if one attributes a virtual mass to the bubble which corresponds to the liquid mass moving around the cavity. Since axial jets are always associated with bubble migration in the direction of the jet, their occurrence and direction can be predicted by analysing the Kelvin impulse at the end of the bubble collapse (Benjamin & Ellis 1966; Gibson & Blake 1982; Blake *et al.* 1986, 1987). Two axial jets in opposite directions arising from an annular jet can, however, develop even when the total Kelvin impulse is zero (Robinson & Blake 1994; Blake *et al.* 1997*a*). As already mentioned, there is a transition from a symmetric annular jet flow creating two equally strong axial jets to a one-directional axial jet flow when one of two opposing pressure gradients becomes dominant. The Kelvin impulse is thus a measure of the difference in strength between the axial jets in opposite directions.

According to the present results, a bubble oscillating near an elastic boundary achieves a zero Kelvin impulse in the bubble splitting region at a γ-value between 0.74 and 0.84 where two nearly equal-sized cavities are formed. The two cavities moving in opposite direction after bubble splitting have Kelvin impulses with equal absolute value, so that the net impulse of the two-bubble system is zero. With decreasing γ, the foot of the mushroom-like shape of the bubble becomes larger and larger and, hence, also the Kelvin impulse towards the boundary.

The simple analysis based on the Kelvin impulse does not portray the whole complexity of the transition from symmetric annular jets to purely axial jets, because it only considers the difference in the axial component of jet formation. The same is true for streak photographic observations of the movement of the lower and upper bubble walls as performed by Shima *et al.* (1989). The real wealth of phenomena can only be revealed by high-speed photography as done in the present study, and by two-dimensional or three-dimensional numerical simulations (Blake *et al.* 1997*a*; Chapyak & Godwin 1998).

In our investigations, the highest jet velocities were observed in the γ-interval $0.5 < \gamma < 0.8$, i.e. close to the γ-value for zero Kelvin impulse where the bubble splitting leads to two equally strong jets in opposite directions. This implies that caution should be used when applying the Kelvin impulse concept to the analysis of the damage potential of bubble dynamics.

4.4. *Cavitation erosion and cavitation-enhanced ablation*

A specific feature of the cavitation bubble interaction with an elastic boundary is that not only the bubble but also the boundary changes shape, and that these changes are interdependent. At intermediate γ-values, the bubble–boundary interaction leads to high-speed liquid jets which can penetrate the sample even when protected by a thin water layer. At $\gamma = 0.6$, for example, the jet penetrated the sample through a water layer of 0.35 mm thickness. At small γ-values, a PAA jet is created by the rebound of the deformed boundary which ejects PAA material into the liquid. Jet-like material ejection after laser-induced bubble formation at a gelatine surface has already been reported by Chapyak & Godwin (1998) who performed numerical simulations of the bubble dynamics occurring during laser thrombolysis for the case of $\gamma = 0$. Our paper, however, presents the first systematic study of the parameter dependence of this phenomenon. The PAA jet resembles a Birkhoff or Munroe jet (Birkhoff *et al.* 1948; Bowden 1966). Later, during the collapse of the cavitation bubble, a volcano-like elevation is formed at the PAA surface. Whereas the PAA jet originates from the rebound of the elastic boundary after its deformation by the expanding cavitation bubble, the volcano-like uplifting of the PAA surface is caused by the collapse of the cavitation bubble. PAA jet formation and uplifting of the boundary are, hence, two different phenomena.

An important result of this work is that cavitation erosion of elastic boundaries is caused not only by the impact of a high-speed liquid jet onto the boundary but also by the material ejection from the boundary. The PAA jet formation and material ejection from the boundary requires that the plastic flow stress of the material is exceeded.

FIGURE 15. Scanning electron micrographs of the lesion produced by the interaction of a laser-induced cavitation bubble with a cornea specimen. The direction of the laser light is parallel to the surface of the cornea, the laser focus was located at the endothelial side of the cornea. (*a*) $\gamma = 0.45$ and (*b*) $\gamma = 0.6$. The white bars represent 100 μm. Figure adapted from Vogel *et al.* (1990).

(*a*)

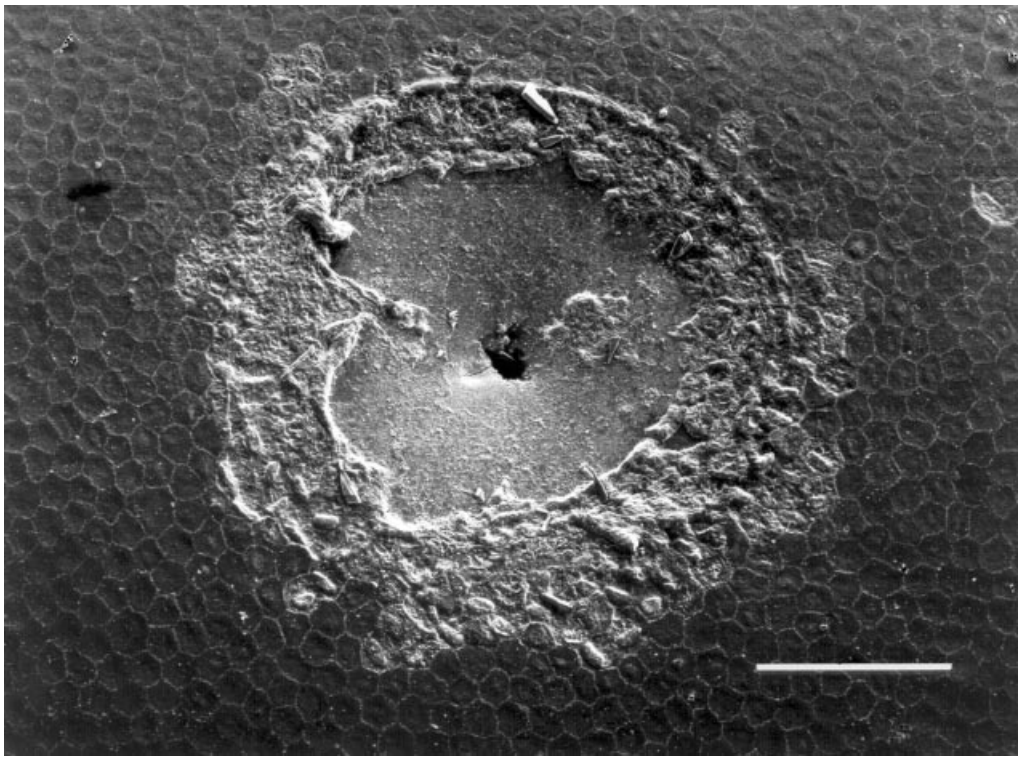

(*b*)

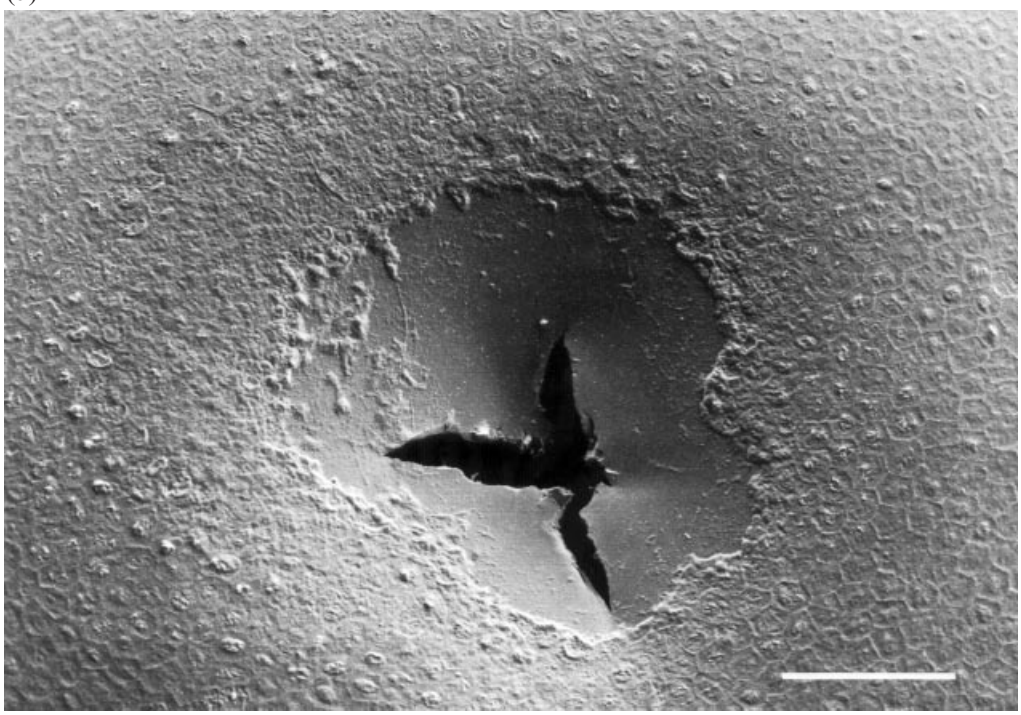

FIGURE 15. For caption see facing page.

Generation of the PAA jet is therefore a threshold phenomenon. This creates a certain irregularity of PAA jet formation in the range of γ-values where the maximum stress values reached inside the PAA material are close to the threshold value. A similar argument applies to the penetration of the PAA sample by the impinging liquid jet. When the impact stresses produced remain slightly below the plastic flow stress, no effect is observed even though the impact velocity of the liquid jet may still be fairly high. At intermediate γ-values, the PAA jet and the liquid jet interfere with one another. The PAA jet is formed first, and therefore sometimes inhibits the liquid jet penetration into the PAA. In cases where no PAA jet develops, however, the liquid jet penetration can be exceptionally deep. The interference of both phenomena explains the variability of the measurement results in figure 14.

The interaction of a laser-induced cavitation bubble with a biological tissue differs markedly from the interaction between a bubble and a solid wall, because the bubble can cause relatively large elastic deformations of the tissue, and the plastic flow stress is easily exceeded. Damage can be easily produced when the tissue surface consists of sensitive cellular structures. This is the case, for example, for the corneal endothelium which is exposed to cavitation effects during intraocular laser surgery (Vogel *et al.* 1990). When the cornea experiences small deformations, the value of the elastic modulus is $E = 0.3$–0.5 MPa (Hoeltzel *et al.* 1992), i.e. quite close to the value of 0.25 MPa for the PAA samples investigated in the present study. Therefore, a comparison of earlier investigations on cavitation-induced corneal damage with the results presented here seems appropriate. Figure 15 shows two lesions caused by the collapse of a laser-induced bubble near the corneal endothelium (a layer of polygonal cells extended over the inner surface of the cornea) for $\gamma = 0.6$ and $\gamma = 0.45$, respectively (Vogel *et al.* 1990). In both lesions, a central rupture in Descemet's membrane (the next layer below the endothelium) is visible which is most likely caused by the impact of the high-velocity liquid jet formed after bubble splitting. Around the central crater there is a zone where the endothelial cell layer is removed, and further outside another zone where the cells are still present, but damaged. These effects are probably caused by the shearing forces arising during the radial jet flow on the corneal endothelium after its impact, and by the tensile stress acting on the cornea during the elevation of its surface upon bubble collapse. Besides these, the high pressure and temperature developed inside the collapsing bubble are also potential cell damage mechanisms. It is interesting to note here that a similar damage pattern was also observed by Bowden & Brunton (1961) as a result of water jet impact onto elastomer surfaces.

The diameter of the hole in Descemet's membrane created by the jet impact at $\gamma = 0.45$ (figure 15*a*) is 20–30 μm and probably similar to the diameter of the jet itself. It amounts to only 1/60 of the maximum bubble diameter. This observation agrees well with the result of the present study that very thin jets are produced during bubble collapse near elastic boundaries. At $\gamma = 0.6$ (figure 15*b*), no hole is produced in Descemet's membrane, but the membrane is ruptured by the jet impact. For $\gamma > 0.8$ no rupture was observed after single-laser pulses (Vogel *et al.* 1990), in good agreement with the result in figure 14 that no liquid jet penetration of the PAA sample occurs for $\gamma > 0.7$. The reason is that for $\gamma > 0.7$ the boundary is protected by a water layer, and no jet towards the boundary is formed for $\gamma > 0.8$. Interestingly, lesions of the corneal endothelial cells were observed up to a dimensionless stand-off distance of $\gamma = 1.2$. For $\gamma = 1.2$, the liquid jet formed during bubble collapse is directed away from the boundary but the surface is still slightly deformed by the tensile stress created upon bubble collapse (see figure 3*b*). We can conclude that the collateral mechanical effects

induced during intraocular laser surgery can be explained well by the interaction of the laser-induced cavitation bubble with neighbouring elastic tissue structures.

The bubble–boundary interaction also plays a role in the efficiency of pulsed laser ablation. Both the jet-like ejection of material into the liquid and the volcano-like uplifting of the surface may directly contribute to material ablation, particularly for materials with small elastic modulus and plastic flow stress (see Brujan *et al.* 2001). The liquid jet towards the boundary contributes indirectly to ablation by weakening the mechanical structure when it penetrates the boundary.

5. Conclusions

The behaviour of a laser-induced cavitation bubble near an elastic boundary as well as the deformation of the boundary induced by bubble motion have been investigated by high-speed photography and acoustic measurements. The elastic boundary consisted of a polyacrylamide (PAA) gel with 80% water concentration with elastic modulus $E = 0.25\,\mathrm{MPa}$.

The interaction of cavitation bubbles with elastic materials is very complex. A large variation in both the jetting behaviour and the deformation of the elastic material is observed depending on the distance between bubble and boundary.

A dominant feature of the bubble dynamics near elastic boundaries is the formation of an annular jet leading to bubble splitting and the formation of two very fast axial jets directed opposite to each other. The formation of annular jets is a consequence of the oblate spheroidal shape of the expanded cavitation bubble which, in turn, is caused by the elastic rebound of the boundary surface after the deformation by the expanding cavitation bubble. The maximum velocity of the axial jet directed towards the boundary was $960\,\mathrm{m\,s^{-1}}$. This jet penetrated the boundary even through a water layer of 0.35 mm thickness. The high jet velocity is the result of three factors: (i) strong focusing of the liquid flow of a slightly asymmetric equatorial jet into a very thin axial jet, (ii) impingement of the shock waves emitted upon the collapse of the cap and neck of the mushroom-shaped bubble on the cavity closer to the boundary, and (iii) the conical shape of this cavity which allows a continuous acceleration of the jet until its tip hits the opposite cavity wall.

A prominent feature of the surface dynamics is the elastic rebound of the boundary surface after the deformation by the expanding cavitation bubble which can result in a jet-like ejection of boundary material into the surrounding liquid. Further material loss from the elastic boundary can occur as a consequence of the tensile stress exerted by the collapsing cavitation bubble.

Liquid jet penetration into the elastic material, the jet-like ejection of boundary material, and the tensile stress from the collapsing bubble may all contribute to the ablation process in short-pulsed laser surgery. If very fine effects merely consisting of tissue evaporation are desired, they can, on the other hand, cause unwanted collateral damage. In engineering, the covering of rigid structures with elastic materials does not seem to be a suitable way of preventing cavitation erosion.

Dr Brujan's stay at the Medical Laser Center Lübeck as well as a part of the computer facilities were sponsored by a grant of the Volkswagen Foundation (Grant No. 960.4-285). We thank Dr Wolfgang Köller of Medical University Lübeck for performing the measurements of the mechanical properties of the PAA samples, and appreciate valuable discussions on the bubble-induced deformation of the PAA surface with Dr Robert P. Godwin of Los Alamos National Laboratory.

REFERENCES

Benjamin, T. B. & Ellis, A. T. 1966 The collapse of cavitation bubbles and the pressures thereby produced against solid boundaries. *Phil. Trans. R. Soc. Lond.* A **260**, 221–240.

Birkhoff, G., Macdougall, D. P., Pugh, E. M. & Taylor, G. 1948 Explosives with lined cavities. *J. Appl. Phys.* **19**, 563–582.

Blake, J. R. & Gibson, D. C. 1987 Cavitation bubbles near boundaries. *Ann. Rev. Fluid Mech.* **19**, 99–123.

Blake, J. R., Hooton, M. C., Robinson, P. B. & Tong, R. P. 1997*a* Collapsing cavities, toroidal bubbles and jet impact. *Phil. Trans. R. Soc. Lond.* A **355**, 537–550.

Blake, J. R., Robinson, P. B., Shima, A. & Tomita, Y. 1993 Interaction of two cavitation bubbles with a rigid boundary. *J. Fluid Mech.* **255**, 707–721.

Blake, J. R., Taib, B. B. & Doherty, G. 1986 Transient cavities near boundaries. Part 1. Rigid boundary. *J. Fluid Mech.* **170**, 479–497.

Blake, J. R., Taib, B. B. & Doherty, G. 1987 Transient cavities near boundaries. Part 2. Free surface. *J. Fluid Mech.* **181**, 197–212.

Blake, J. R., Tomita, Y. & Tong, R. P. 1997*b* The art, craft and science of modelling jet impact in a collapsing cavitation bubble. *Appl. Sci. Res.* **58**, 77–90.

Bowden, F. P. 1966 The formation of microjets in liquids under the influence of impact or shock. *Phil. Trans. R. Soc. Lond.* A **260**, 94–95.

Bowden, F. P. & Brunton, J. H. 1961 The deformation of solids by liquid impact at supersonic speeds. *Proc. R. Soc. Lond.* A **263**, 433–450.

Brinkmann, R., Theisen, D., Brendel, T. & Birngruber, R. 1999 Single-pulse 30-J holmium laser for myocardial revascularization – A study on ablation dynamics in comparison to CO_2 laser-TMR. *IEEE J. Selected Topics Quantum Electron.* **5**, 1–12.

Brujan, E. A., Nahen, K., Schmidt, P. & Vogel, A. 2001 Dynamics of laser-induced cavitation bubbles near elastic boundaries: Influence of the elastic modulus. *J. Fluid Mech.* **433**, 283–314.

Chahine, G. L. 1982 Experimental and asymptotic study of nonspherical bubble collapse. *Appl. Sci. Res.* **38**, 187–197.

Chapman, R. B. & Plesset, M. S. 1972 Nonlinear effects in the collapse of a nearly spherical cavity in a liquid. *Trans. ASME* D: *J. Basic Engng* **94**, 142–145.

Chapyak, E. J. & Godwin, R. P. 1998 Physical mechanisms of importance to laser thrombolysis. *SPIE Proc.* **3245**, 12–18.

Dear, J. P., Field, J. E. & Walton, A. J. 1988 Gas compression and jet formation in cavities collapsed by a shock wave. *Nature* **332**, 505–508.

Deckelbaum, L. I. 1994 Coronary laser angioplasty. *Lasers Surg. Med.* **14**, 101–110.

Duck, F. A. 1990 *Physical Properties of Tissue*. Academic.

Duncan, J. H., Milligan, C. D. & Zhang, S. 1996 On the interaction between a bubble and a submerged compliant structure. *J. Sound Vib.* **197**, 17–44.

Duncan, J. H. & Zhang, S. 1991 On the interaction of a collapsing cavity and a compliant wall. *J. Fluid Mech.* **226**, 401–423.

Fung, Y. C. 1993 *Biomechanics. Mechanical Properties of Living Tissues*. Springer.

Gibson, D. C. 1968 Cavitation adjacent to plane boundaries. In *Proc. 3rd Australasian Conf. on Hydraulics and Fluid Mechanics, Sydney*, pp. 210–214. The Institution of Engineers, Australia.

Gibson, D. C. & Blake, J. R. 1980 Growth and collapse of cavitation bubbles near flexible boundaries. In *Proc. 7th Australasian Conf. on Hydraulics and Fluid Mechanics, Brisbane*, pp. 283–286. The Institution of Engineers, Australia.

Gibson, D. C. & Blake, J. R. 1982 The growth and collapse of bubbles near deformable surfaces. *Appl. Sci. Res.* **38**, 215–224.

Godwin, R. P., Chapyak, E. J., Noack, J. & Vogel, A. 1999 Aspherical bubble dynamics and oscillation times. *SPIE Proc.* **3601**, 225–237.

Gregory, K. W. 1994 *Laser Thrombolysis*. Saunders.

Hoeltzel, D. A., Altmann, P., Buzard, K. & Choe, K.-I. 1992 Strip extensiometry for comparison of the mechanical properties of bovine, rabbit, and human corneas. *Trans. ASME* E: *J. Biomech. Engng* **114**, 202–215.

Klein, M., Schulte, H. D. & Gams, E. 1998 *TMLR Management of Coronary Artery Diseases*. Springer.

KODAMA, T. & TOMITA, Y. 2000 Cavitation bubble behaviour and bubble-shock wave interaction near a gelatin surface as a study of in vivo bubble dynamics. *Appl. Phys.* B **70**, 139–149.

LAUTERBORN, W. 1982 Cavitation bubble dynamics – new tools for an intricate problem. *Appl. Sci. Res.* **38**, 165–178.

LAUTERBORN, W. & HENTSCHEL, W. 1985 Cavitation bubble dynamics studied by high speed photography and holography: part one. *Ultrasonics* **23**, 260–267.

NAUDÉ, C. F. & ELLIS, A. T. 1961 On the mechanism of cavitation damage by nonhemispherical cavities collapsing in contact with a solid boundary. *Trans. ASME* D: *J. Basic Engng* **83**, 648–656.

OHL, C. D., PHILIPP, A. & LAUTERBORN, W. 1995 Cavitation bubble collapse studied at 20 million frames per second. *Ann. Physik* **4**, 26–34.

PHILIPP, A., DELIUS, M., SCHEFFCZYK, C., VOGEL, A. & LAUTERBORN, W. 1993 Interaction of lithotripter-generated shock waves with air bubbles. *J. Acoust. Soc. Am.* **93**, 2496–2509.

PHILIPP, A. & LAUTERBORN, W. 1998 Cavitation erosion by single laser-produced bubbles. *J. Fluid Mech.* **361**, 75–116.

PLESSET, M. S. & CHAPMAN, R. B. 1971 Collapse of an initially spherical vapour cavity in the neighbourhood of a solid boundary. *J. Fluid Mech.* **47**, 283–290.

RAYLEIGH, LORD 1917 On the pressure developed in a liquid during the collapse of a spherical cavity. *Phil. Mag.* **34**, 94–98.

ROBINSON, P. B. & BLAKE, J. R. 1994 Dynamics of cavitation bubble interactions. In *Proc. IUTAM Symp. 'Bubble Dynamics and Interface Phenomena'* (ed. J. R. Blake *et al.*), pp. 55–64. Kluwer.

SHAW, S. J., JIN, Y. H., GENTRY, T. P. & EMMONY, D. C. 1999 Experimental observations of the interaction of a laser-generated cavitation bubble with a flexible membrane. *Phys. Fluids* **11**, 2437–2439.

SHIMA, A., TOMITA, Y., GIBSON, D. C. & BLAKE, J. R. 1989 The growth and collapse of cavitation bubbles near composite surfaces. *J. Fluid Mech.* **203**, 199–214.

SMITH, C. F. 1993 Lasers in orthopedic surgery. *Orthopedics* **16**, 451–534.

STEINERT, R. F. & PULIAFITO, C. A. 1985 *The Nd:YAG Laser in Ophthalmology*. Saunders.

TOMITA, Y., SATO, K. & SHIMA, A. 1994 Interaction of two laser-produced cavitation bubbles near boundaries. In *Proc. IUTAM Symp. 'Bubble Dynamics and Interface Phenomena'* (ed. J. R. Blake *et al.*), pp. 33–45. Kluwer.

TONG, R. P., SCHIFFERS, W. P., SHAW, S. J., BLAKE, J. R. & EMMONY, D. C. 1999 The role of 'splashing' in the collapse of a laser-generated cavity near a rigid boundary. *J. Fluid Mech.* **380**, 339–361.

VOGEL, A. 1997 Nonlinear absorption: intraocular microsurgery and laser lithotripsy. *Phys. Med. Biol.* **42**, 895–912.

VOGEL, A., BUSCH, S. & PARLITZ, U. 1996*a* Shock wave emission and cavitation bubble generation by picosecond and nanosecond optical breakdown in water. *J. Acoust. Soc. Am.* **100**, 148–165.

VOGEL, A., LAUTERBORN, W. & TIMM, R. 1989 Optical and acoustic investigations of the dynamics of laser-produced cavitation bubbles near a solid boundary. *J. Fluid Mech.* **206**, 299–338.

VOGEL, A., NAHEN, K., THEISEN, D. & NOACK, J. 1996*b* Plasma formation in water by picosecond and nanosecond Nd:YAG laser pulses – Part I: Optical breakdown at threshold and superthreshold irradiance. *IEEE J. Selected Topics Quantum Electron.* **2**, 847–860.

VOGEL, A., SCHWEIGER, P., FRIESER, A., ASIYO, M. N. & BIRNGRUBER, R. 1990 Intraocular Nd:YAG laser surgery: light tissue interaction, damage range, and reduction of collateral effects. *IEEE J. Quantum Electron.* **26**, 2240–2260.

VOINOV, O. V. & VOINOV, V. V. 1976 On the process of collapse of a cavitation bubble near a wall and the formation of accumulative jet. *Sov. Phys. Dokl.* **21**, 133–135.